Author's accepted version of the paper published in Mechanical Systems and Signal Processing 185 (2023) 109799 https://doi.org/10.1016/j.ymssp.2022.109799

Parameter, Input and State Estimation for Linear Structural Dynamics using parametric Model Order Reduction and Augmented Kalman Filtering

Cristian Enrico Capalbo[a,b], Daniel De Gregoriis[b], Tommaso Tamarozzi[b], Hendrik Devriendt[c,d], Frank Naets[c,d], Giuseppe Carbone[a], Domenico Mundo[a]

[a] *Department of Mechanical, Energy and Management Engineering, University of Calabria, Cubo 45C, Rende, 87036, Italy*
[b] *Siemens Industry Software NV, Interleuvenlaan 68, Leuven, B-3001, Belgium*
[c] *Department of mechanical engineering, KU Leuven, Celestijnenlaan 300 B, Heverlee, B-3001, Belgium*
[d] *DMMS core lab, Flanders Make @ KU Leuven, Gaston Geenslaan 8, Heverlee, 3001, Belgium*

Abstract

Tracking the evolution in time of parameters, input and states of a structural dynamic system is often difficult, since their direct measurement can be problematic or even impossible. It is of great interest to estimate these quantities based on output-only data from a limited set of sensors. This work proposes an estimation technique for states, inputs and material parameters for structural dynamics models based on an Augmented Extended Kalman Filter. A parametric Model Order Reduction technique is proposed to construct a Reduced Order Model which maintains an explicit dependency on material parameters, enabling the parameter estimation thanks to a low computational cost and an efficient derivation of the linearized system. The choice of sensor configurations that ensure the observability of unknown quantities is discussed as well. The proposed methodology shows highly promising results and could be employed for model refinement or condition monitoring. The methodology is validated both numerically and experimentally, using data acquired on a scaled wind turbine blade, with errors on the estimated parameters lower than 3.5% with respect to experimentally identified parameter values.

Keywords: Structural dynamics, Parameter-input-state estimation, Parametric model order reduction, Augmented extended Kalman filter, Parameter identification

1. Introduction

Parameter identification [1, 2] and tracking [3, 4] have been among the main research interests in structural dynamics over the last years. The system's states are also commonly tracked to have a complete knowledge about the system evolution in time. In most cases, parameters and states are difficult to directly measure. The main limiting factors are, among others, the high cost of the required sensors and mounting inaccessibility, potential interference with operations or, at times, appropriate sensors might not even exist. A common approach to overcome these issues is employing indirect estimation methods, that are typically based on the measurement of a set of responses of the system to known inputs. Often however, measuring these inputs is also not straightforward. Therefore, ideally an output-only procedure should be employed, where the estimation of parameters and states is coupled with the concurrent estimation of inputs.

A well known estimation approach, originally developed for state estimation, is the Kalman Filter (KF) [5, 6], which combines a numerical model of the system and measured sensor data by minimizing the trace of the state error covariance matrix. For non-linear systems, several variations have been proposed in literature, such as e.g. the Extended Kalman Filter (EKF) [6] and the Sigma-Point Kalman Filters (SPKF) [7]. In order to simultaneously estimate inputs and parameters, common approaches are Dual Kalman Filters (DKF) [8, 9] or state augmentation [10]. DKF consists of two separate filters estimating the states and the unknown quantities in parallel. State augmentation consists instead of extending, i.e. augmenting, the system state vector with the unknown quantities such as e.g. inputs or parameters. This approach allows to keep into account all coupling effects between the estimated quantities, given that the augmented system is observable [11]. Furthermore, it generally results in a gain in computational time. A zeroth order random walk model is often used to model the augmented states dynamics [12, 13]. By employing one of these two techniques, several authors jointly estimated states and inputs [13, 14, 15], states and parameters [16, 17, 18, 9] or the three together [12, 19, 20, 21].

For structural dynamics applications, KF approaches typically use Finite Element (FE) models, that can have a large number of Degrees of Freedom (DOFs); i.e. in the order of hundreds of thousands up to millions. The direct use of these models can result in an unfeasible computational load. Their dimensions are usually reduced by employing projection-based Model Order Reduction (MOR) techniques [22, 23, 24]. Here, the governing equations of the Full Order Model (FOM) are projected onto a lower dimensional subspace of the solution space, the so-called reduction space, which is spanned by a reduction basis. This effectively reduces both the number of equations and DOFs, resulting in a so-called Reduced Order Model (ROM) with a decreased associated computational load.

When using a KF for parameter estimation, the parameter values are updated at each time step, requiring the model to be updated accordingly. Since in general ROMs do not retain any explicit parametric dependency, it is necessary to recreate the ROM at each step, which could result in a loss of most of the computational efficiency granted by the use of a ROM in the first place. This explicit dependency can however be retained by applying a parametric Model Order Reduction (pMOR) technique. A comprehensive overview on projection-based pMOR techniques can be found in the work by Benner et al. [25]. The usage of pMOR for model identification together with optimization methods has been proposed in literature [26, 27]. Employing a parametric Reduced Order Model (pROM) inside a KF-based parameter estimation allows to efficiently update the model for each new estimated parameter value, resulting in an overall computationally efficient procedure. This approach has been proposed by Naets et al. [12] for the joint estimation of states, parameters and input in linear structural dynamics applications. Here, the employed pMOR scheme consists of the interpolation of ROMs which have been calculated for different sampled parameter values, which can be seen as a *local* approach [25]. By not assuming any particular form for the parametric dependency of the full model, this approach allows to have a general representation for a large variety of parameters. This causes a loss of information about the kind of parameters considered, and the form of parametric dependency is not fully exploited. The downside of the local approach is that a ROM and its reduction basis have to be calculated and stored for each parameter sample, potentially resulting in a large computational overhead. The interpolation of the ROMs and reduction bases introduces further computational bottlenecks. In order to guarantee the consistency of the different reduced sets of DOFs, an intermediate projection to a high-dimensional space is typically required.

This work proposes an augmented EKF framework which uses a pMOR approach that exploits models with an affine parameter dependency and uses a constant global reduction basis [25]. More specifically, linear structural FE models show an affine dependency on material parameters. In this case, a global reduction basis, i.e. not depending on parameters, can be defined and used to reduce the so-called affine components in an off-line phase. The evaluation of the parametric model becomes then straightforward in the on-line phase [28]. Only one global basis and a small set of matrices - the affine components - thus have to be stored, leading to significant gains with respect to storage and a positive impact on the computational performances. The proposed framework enables the efficient joint estimation of states, inputs and parameters. Furthermore, the proposed pMOR approach preserves the structure of the FOM parametric dependency, allowing to distinguish between different types of parameters (e.g. stiffness-related and mass-related) and consequently to analyze their observability individually.

The paper is structured as follows: in section 2 the affine representation for the structural FE system matrices is derived, and the proposed pMOR scheme is described and validated. In section 3 the EKF is described and in section 4 the influence of the type of measurements and estimated quantities on the system observability is highlighted. An extensive numerical validation of the estimation procedure is presented in section 5. An experimental validation of the proposed approach is presented in section 6. Finally, conclusions are given in section 7.

2. Parametric Model Order Reduction for Finite Element structural models

For a parametric linear structural FE model, the semi-discrete (continuous in time, discrete in space) Equations Of Motion (EOM) of the FOM can be written as:

$$\mathbf{M}(\mathbf{p})\ddot{\mathbf{z}} + \mathbf{C}(\mathbf{p})\dot{\mathbf{z}} + \mathbf{K}(\mathbf{p})\mathbf{z} = \mathbf{S}\mathbf{u} \tag{1}$$

where $\mathbf{z} \in \mathbb{R}^{n_{dof}}$ are the nodal DOFs, $\mathbf{M}$, $\mathbf{C}$ and $\mathbf{K}$ are respectively the stiffness, damping and mass matrices, $\mathbf{S}$ is the input shape matrix that distributes the external forces $\mathbf{u} \in \mathbb{R}^{n_f}$ on the DOFs of the system and $\mathbf{p} \in \mathbb{R}^{n_p}$ are the parameters of the system. In this work the parameters of interest are material properties such as Young's modulus (E), density (ρ) and Poisson's ratio (ν) for isotropic materials. Each of the EOM components is dependent on time, but has been omitted from notation for clarity purposes. The EOM are generally derived by assuming constant mass for the system, while if the density is time-variant an additional related term appears in the equations [29]. The assumption made in this work is that density varies slowly in time, a realistic behavior for system identification or monitoring applications, so that the additional term is assumed to be negligible.

2.1. Affine Representation

The system matrices should exhibit an affine dependency on the considered parameters to guarantee the efficiency of the global basis pMOR approach. The affine representation for a generic matrix $\mathbf{X}(\mathbf{p})$ can be stated as:

$$\mathbf{X}(\mathbf{p}) = \mathbf{X}_0 + \sum_i \mathbf{X}_i f_i(\mathbf{p}) \tag{2}$$

where $\mathbf{X}_0$ is the constant term, $\mathbf{X}_i$ are the affine components and $f_i(\mathbf{p})$ are the affine functions.

In the following sections, the affine representation of the matrices of the system is explicitly described. The FE formulation employed in this section is based on [30].

Stiffness Matrix parameterization

The constitutive relationship for an isotropic material links the stress vector $\boldsymbol{\sigma} \in \mathbb{R}^6$ and strain vector $\boldsymbol{\epsilon} \in \mathbb{R}^6$ through the constitutive matrix $\mathbf{E} \in \mathbb{R}^{6\times 6}$. This matrix has an affine relationship with the Young's modulus E and Poisson coefficient ν of the material:

$$\mathbf{E} = \begin{bmatrix} \mathbf{1} & \mathbf{0} \\ \mathbf{0} & \mathbf{0} \end{bmatrix} \frac{E\nu}{(1+\nu)(1-2\nu)} + \begin{bmatrix} 2\mathbf{I} & \mathbf{0} \\ \mathbf{0} & \mathbf{I} \end{bmatrix} \frac{E}{2(1+\nu)} = \mathbf{E}^{\lambda}\lambda + \mathbf{E}^{\mu}\mu \tag{3}$$

where λ and μ are the Lamé parameters.

In the former equation and in the following $\mathbf{I}$, $\mathbf{0}$ and $\mathbf{1}$ represent respectively the identity matrix, the zero matrix and the all-ones matrix of appropriate dimensions.

If the material properties are assumed constant over the element volume, the same parameter dependence as in Equation 3 applies for the element stiffness matrix $\mathbf{K}_e$:

$$\mathbf{K}_e = \mathbf{K}_e^{\lambda}\lambda + \mathbf{K}_e^{\mu}\mu \tag{4}$$

The corresponding assembled system stiffness matrix $\mathbf{K}$ retains the parametric relationship.

From Equation 4 it is clear that the two Lamé parameters themselves are the needed affine functions if the system is parameterized for both E and ν. It can be shown in an equivalent way that E is itself the affine function needed if ν is not considered in the parameterization. The final affine representation of the parametric stiffness matrix for a model containing multiple materials is then:

$$\mathbf{K}(\mathbf{p}) = \mathbf{K}_0 + \sum_i [\mathbf{K}_i^{\lambda}\lambda_i + \mathbf{K}_i^{\mu}\mu_i] + \sum_j \mathbf{K}_j^{E} E_j \tag{5}$$

where $\lambda_i = \lambda(E_i, \nu_i)$ and $\mu_i = \mu(E_i, \nu_i)$. The materials represented by an index i are parameterized for both E and ν, while the ones represented by an index j are only parameterized for E. $\mathbf{K}_0$ is a constant term accounting for possible terms that do not depend on parameters (if for example some of the materials in the model are not parameterized). The approach could be easily generalized to take into account localized stiffness terms related to lumped spring elements.

Mass Matrix parameterization

The consistent mass matrix of a single element, assuming constant material parameters over the volume, can be represented with an affine dependency on the material density ρ as:

$$\mathbf{M}_e = \mathbf{M}^{\rho}\rho \tag{6}$$

Following the same considerations made for the stiffness matrix, the affine representation of the parameterized mass matrix for a model containing multiple materials is:

$$\mathbf{M}(\mathbf{p}) = \mathbf{M}_0 + \sum_i \mathbf{M}_i^{\rho}\rho_i \tag{7}$$

where $\mathbf{M}_0$ is a constant term accounting for eventual terms that do not depend on parameters (such as non-parameterized lumped masses or materials).

Damping Matrix parameterization

A typical and well known approach to model damping in structural applications is the proportional Rayleigh damping model. This consists in defining the damping matrix as a linear combination of mass and stiffness matrices as:

$$\mathbf{C}(\mathbf{p}) = \alpha\mathbf{M}(\mathbf{p}) + \beta\mathbf{K}(\mathbf{p}). \tag{8}$$

where α and β are the Rayleigh damping parameters.

This model has the advantage of retaining the parametric dependencies for the damping matrix.

Affine Component Extraction

Starting from a set of matrices calculated at n_s different parameter values, the so-called sampling points, a least squares problem is solved to calculate the affine components. For a generic matrix, given the samples $[\mathbf{p}^1 ... \mathbf{p}^{n_s}]$ and the corresponding matrices $[\mathbf{X}^1 ... \mathbf{X}^{n_s}]$, the affine components are calculated by solving for each element $X_{(a,b)}$ of the matrices:

$$\min_{X_{0(a,b)},\dots,X_{i(a,b)},\dots} \sum_{h=1}^{n_s} \left\| X^h_{(a,b)} - X_{0(a,b)} - \sum_i X_{i(a,b)} f_i(\mathbf{p}^h) \right\| \tag{9}$$

where i represents the affine component index, as in Equation 2. In the former equation and in the rest of the paper, $\|\cdot\|$ denotes the L^2 norm. This procedure requires the sampling of the FOM a number of times at least equal to the number of components to be identified. An n_s lower than the number of unknowns in the least squares problem would in fact results in an underdetermined problem. The full matrices can be stored and used for identification during the sampling phase of the pROM creation (described below) at a minimum added computational cost.

2.2. pMOR Scheme

The DOFs vector $\mathbf{z}$ is approximated by projecting it onto a lower-dimension subspace spanned by the global basis $\mathbf{\Psi} \in \mathbb{R}^{n_{dof} \times n_{red}}$ that, given the pMOR scheme employed, is constant and does not depend on time or on the value of the parameters of interest:

$$\mathbf{z} \approx \mathbf{\Psi q} \tag{10}$$

where $\mathbf{q} \in \mathbb{R}^{n_{red}}$ is the reduced set of DOFs.

The Galerkin projection of the EOM onto the reduced space yields the reduced EOM:

$$\mathbf{M}^r(\mathbf{p})\ddot{\mathbf{q}} + \mathbf{C}^r(\mathbf{p})\dot{\mathbf{q}} + \mathbf{K}^r(\mathbf{p})\mathbf{q} = \mathbf{S}^r\mathbf{u} \tag{11}$$

where $\mathbf{M}^r(\mathbf{p}) = \mathbf{\Psi}^T\mathbf{M}(\mathbf{p})\mathbf{\Psi}$, $\mathbf{C}^r(\mathbf{p}) = \mathbf{\Psi}^T\mathbf{C}(\mathbf{p})\mathbf{\Psi}$, $\mathbf{K}^r(\mathbf{p}) = \mathbf{\Psi}^T\mathbf{K}(\mathbf{p})\mathbf{\Psi}$ and $\mathbf{S}^r = \mathbf{\Psi}^T\mathbf{S}$.

Using Equation 5 and Equation 7, the parametric reduced matrices become:

$$\mathbf{K}^r(\mathbf{p}) = \mathbf{K}^r_0 + \sum_i [\mathbf{K}_i^{r\lambda}\lambda(E_i, \nu_i) + \mathbf{K}_i^{r\mu}\mu(E_i, \nu_i)] + \sum_j \mathbf{K}_j^{rE} E_j \tag{12}$$

$$\mathbf{M}^r(\mathbf{p}) = \mathbf{M}^r_0 + \sum_i \mathbf{M}_i^{r\rho}\rho_i \tag{13}$$

And the reduced damping matrix retains the proportional relationship:

$$\mathbf{C}^r(\mathbf{p}) = \alpha\mathbf{M}^r(\mathbf{p}) + \beta\mathbf{K}^r(\mathbf{p}) \tag{14}$$

Reduction Basis Selection

In this work the global reduction basis $\mathbf{\Psi}$ is constructed by concatenating local bases $\mathbf{\Psi}_i$, corresponding to different parameter samples $\mathbf{p}_i$, and carrying out a subsequent Singular Value Decomposition (SVD) [24].

The reduction basis is representative of the system for a set of configurations that correspond to specific parameters values. This poses the challenge of identifying a global reduction space that properly represents the system's behavior over the range of parameter values of interest. This is particularly true for a modal basis, which contains a subset of the eigenmodes of the system, since the eigenmode shapes can vary greatly for different values of the parameters. The final reduction basis thus has to accurately represent possible deformations across the parameter range in its entirety while having a reasonably small dimension. The steps required for the basis selection are shown in Figure 1, and are further described below.

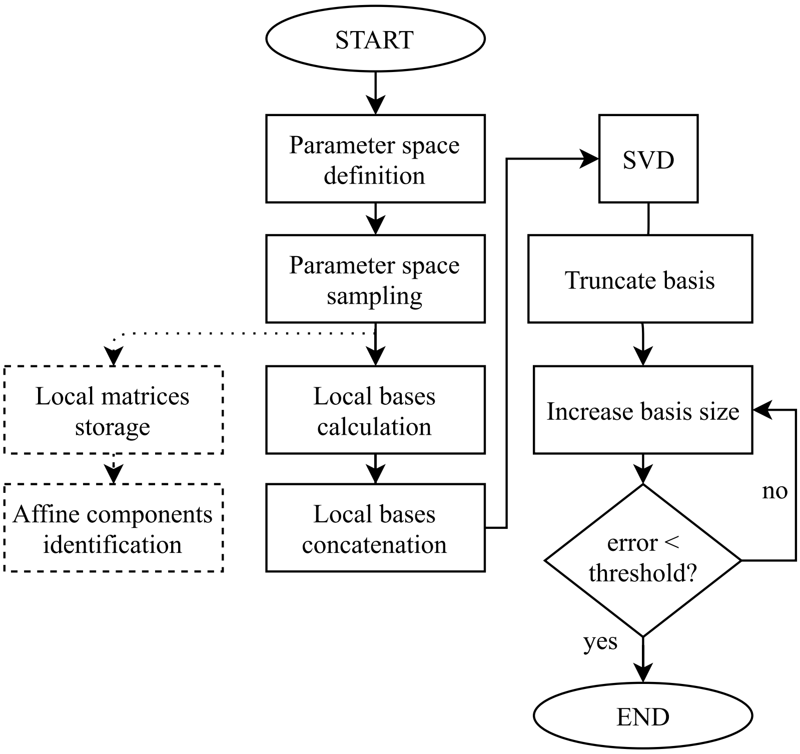

Figure 1: Basis selection workflow

Parameter Space Definition and Sampling

The parameter space $\mathbf{\Omega}$ is defined by setting upper and lower limits for each parameter based on the application of interest: $\mathbf{\Omega} = \{p_i \in \mathbb{R}, p_i^{min} < p_i < p_i^{max} \forall p_i\}$.

Once defined, the parameter space has to be sampled in order to get a set of configurations that is representative of the entire space. Several sampling methods have been proposed in literature for pMOR. Benner et al. [25] state that, for a small or moderate number of parameters ($n_p < 10$), a Latin Hypercube Sampling (LHS) method is effective. Several methods have been tested for the application at hand (e.g. uniform sampling, LHS) and LHS proved to be the most effective. Therefore this method is adopted in this work. In case of a large parameter space, for which the LHS would require a high number of samples, other techniques (such as e.g. greedy sampling [31]) could be adopted.

Local Bases and Matrices Generation

For each parameter sample $\mathbf{p}_i$ the full system, consisting of the matrices $\mathbf{M}_i$ and $\mathbf{K}_i$, is assembled. These FOM matrices are used to extract the corresponding local basis. This basis consists of a set of eigenmodes $\mathbf{\Psi}_{nm,i}$ concatenated with a set of static modes $\mathbf{\Psi}_{sm,i}$ [13, 23], so that $\mathbf{\Psi}_i = \mathbf{\Psi}(\mathbf{p}_i) = [\mathbf{\Psi}_{nm,i}\mathbf{\Psi}_{sm,i}]$. The FOM matrices are stored for the affine component identification as explained in section 2.1.

Global Reduction Basis Construction

The global basis is constructed by concatenating the local bases:

$$\mathbf{\Psi}_{global} = [\mathbf{\Psi}_1 ... \mathbf{\Psi}_{n_s}] \tag{15}$$

In general, this matrix of local bases can have linearly dependent columns. In order to remove these linear dependencies, an SVD is performed:

$$\mathbf{\Psi}_{global} = \mathbf{U}\mathbf{\Sigma}\mathbf{V}^T \tag{16}$$

The Left Singular Vectors (LSVs) $\mathbf{U}$ represent an orthonormal set of vectors that, spanning the range of $\mathbf{\Psi}_{global}$ [24], is suitable to be used as a reduction basis. In order to only keep the vectors that contain most of the information and therefore obtain a global basis of small enough dimension, a subset of the LSVs is used as the global truncated basis $\mathbf{\Psi}$. This truncated LSVs basis exhibits the property of being the optimal low-rank approximation for the full basis [24]. The choice of how many LSVs to retain is done through an iterative procedure that subsequently increases the number of retained basis vectors and compares the Frequency Response Functions (FRFs) of the pROM over a set of n_{in} input DOFs and n_{out} output DOFs and in a specific frequency range until the relative error becomes lower than a user-defined threshold.

Let $H_{ij}(\omega, \mathbf{\Psi}, \mathbf{p})$ be the FRF for the input DOF i and the output DOF j, using the pROM created using the basis $\mathbf{\Psi}$ evaluated for the parameter values $\mathbf{p}$. Furthermore, the frequency range is discretized as $[\omega_1, \, ... \, , \omega_{n_\omega}]$. At each iteration step k, the relative error between the FRFs calculated using the current reduction basis $\mathbf{\Psi}_k$ and the one relative to the previous step $\mathbf{\Psi}_{k-1}$ is calculated as:

$$e_k(\mathbf{p}) = \sum_{i=1}^{n_{in}} \sum_{j=1}^{n_{out}} \left(\frac{1}{n_\omega} \sum_{l=1}^{n_\omega} \frac{\| (\|H_{ij}(\omega_l, \mathbf{\Psi}_{k-1}, \mathbf{p})\| - \|H_{ij}(\omega_l, \mathbf{\Psi}_k, \mathbf{p})\|) \|}{\|H_{ij}(\omega_l, \mathbf{\Psi}_{k-1}, \mathbf{p})\|} \right) \tag{17}$$

This metric allows to achieve a good accuracy of the pROM in the frequency range of interest while limiting the number of evaluations needed for the FRFs to only the set of input/output DOFs. Furthermore, the metric also allows to compare both the shape of the responses and the amplitude. The error can be evaluated on a single parameter configuration of interest or averaged over a set of configurations. In this work, the error is calculated for the parameter values at the center of the sampled range.

2.3. pMOR Numerical Validation

A numerical validation of the proposed pMOR scheme is shown against a standard ROM and is presented below.

The system considered for the validation is a scaled wind turbine blade present at the testing facilities of Siemens Industry Software NV in Leuven (Belgium). The blade consists of Titanium Gr23 and has been produced using additive manufacturing followed by heat treatments. It is fixed to a concrete base via a set of bolted connections to its flange.

The linear FE model of the blade used in this work (Figure 2a) mainly consists of linear hexahedral elements and a minority of linear pentahedral elements, for a total of 65264 nodes and 391584 DOFs. Rigid elements connect the entire face of the flange to four spring elements that model the compliance of the bolts, as shown in Figure 2b.

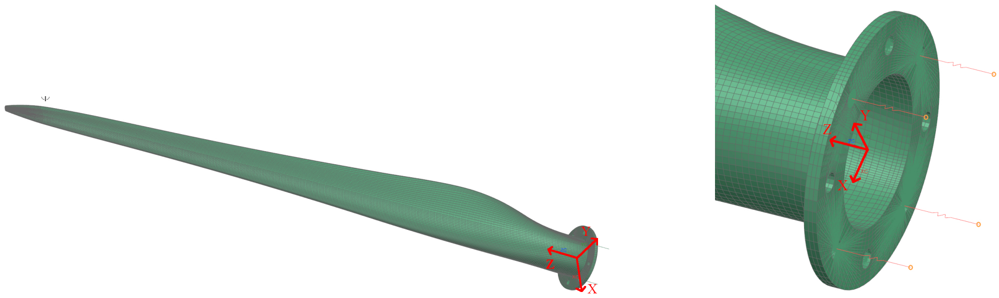

(a) (b)

Figure 2: Finite element model of the blade

The pROM has been created considering the Young's modulus and the density as parameters. This choice aims at giving a smaller set of representative parameters that can be easily represented in results.

A commercial FE solver [32] has been used to extract the full model information needed for the pROM generation. The least-squares procedure identification described in section 2 has been applied for the affine component identification. The settings used for the creation of the pROM can be seen in Table 1. The number of eigenvectors of the structure with an associated eigenfrequency in the range of interest is higher for configurations with low stiffness and high density. The size of the local basis has therefore been chosen to contain the entire set of modes even for these extreme cases. Figure 3 shows the convergence of the relative error in the basis size selection procedure, in which the basis starts with a dimension of 24 and is increased by 12 basis vectors at each iteration. The relative error decreases monotonically to reach a value beyond the threshold in 3 iterations. The final dimension of the pROM is 60, with a reduction factor of more than 6000 with respect to the full model.

Table 1: Blade's pROM information

size of $\mathbf{\Psi}_i$	24 (15 eigenmodes + 9 static modes)
number of samples	5
relative error threshold	10^{-3}
frequency range	0-500Hz
number of nodes	65264
DOFs of the full model	391584
size of $\mathbf{\Psi}_{global}$	60

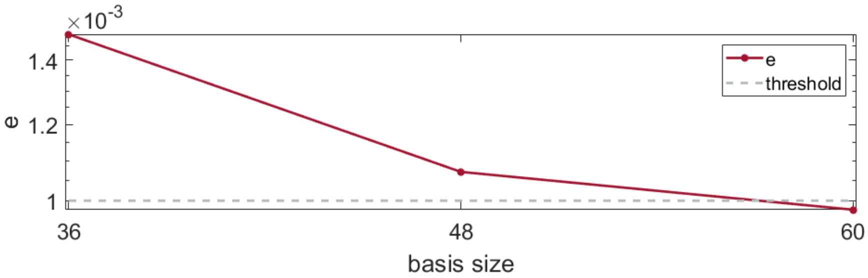

Figure 3: Relative error for the global basis selection iterative procedure of the blade's pROM. The basis size starts at 24 and the first relative error is calculated at the second step where the size increased to 36.

Frequency Domain Analysis

In order to check that the pROM properly interpolates the behavior of the model in the frequency range and parameter space considered, the FRFs can be calculated and compared for a set of input/output DOFs of interest with the ones of the full FE models and non-parametric ROMs created for a specific set of parameters. The results in Figure 4 show the FRFs of a FE model, a standard, non-parametric ROM and the pROM for parameter values not used in the pROM generation, namely the nominal values as well as two extremes of the parameter range, for input and output on the force application point at the bottom face of the blade. A good correspondence can be observed.

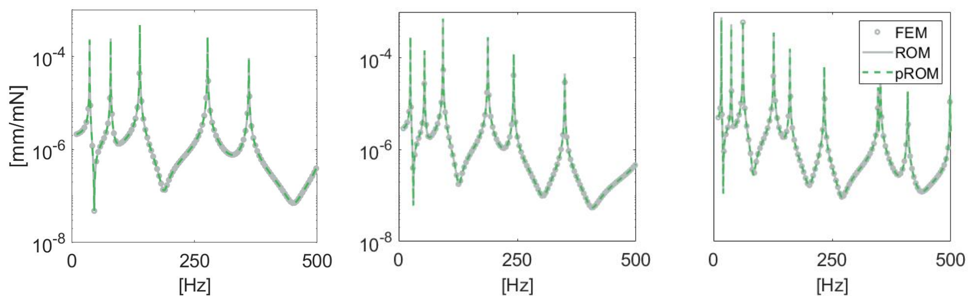

(a) High E and low rho (b) Reference values (c) Low E and high rho

Figure 4: FRFs comparison on 3 parameter sets.

In Figure 5 the average error (calculated as $\frac{|(|FRF_{pROM}|-|FRF_{ROM}|)|}{|FRF_{ROM}|}$) on the FRFs between ROM and pROM is plotted over a parameter range larger than the one used for generating the pROM, corresponding to 11×11 samples. This shows as, in the original range, the interpolation by the pROM is accurate and provides good results even far from sampling points. Outside of the range the error is still low, but it shows a tendency to grow in the low stiffness zone where the frequency range includes a higher number of eigenfrequencies associated with eigenmodes of the structure.

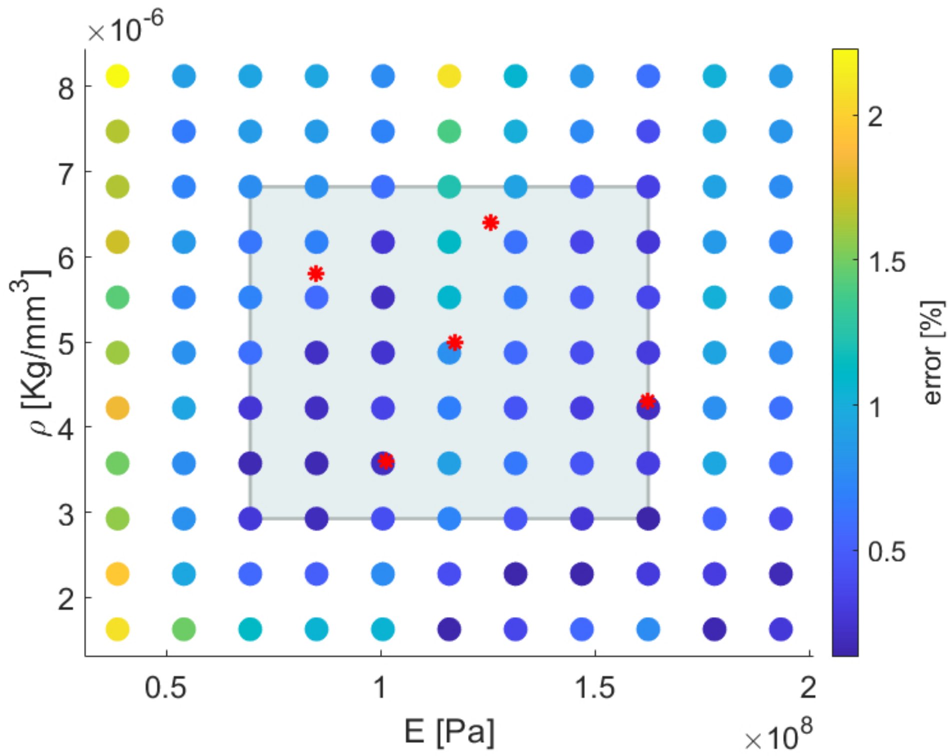

Figure 5: Relative error between ROM and pROM FRFs over the parameter space sampled on a 11x11 grid. The grey box and the red stars are respectively the parameter space and the sampled points used for the pROM generation.

Time Domain Analysis

Since instabilities can arise when employing a ROM for time domain simulations if not handled properly [33, 34], the comparison of FRFs might not be sufficient to properly asses the quality of the proposed pMOR technique. Therefore, a comparison is also carried out in the time domain. The results are shown in Figure 6, where a continuous random signal with a frequency content in the range of 0-500Hz is applied to the pROM. The acceleration is calculated at the same location as the input force, while the strain is calculated at a location on the top face in the direction of the axis of the blade. A first-order implicit Euler time integration scheme was used for the forward simulation presented in this section with an integration step $h = 0.1ms$. A good correspondence between the ROM and pROM can again be observed.

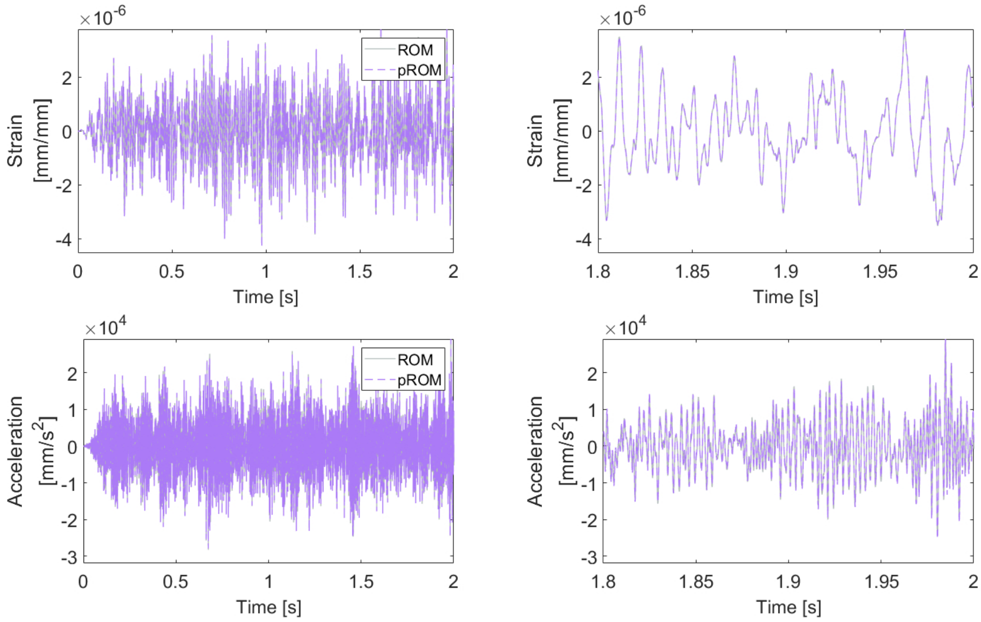

Figure 6: Comparison of time-domain simulations for a continuous random input. The right figures show a zoom of the 1.8s to 2s range.

3. Augmented Extended Kalman Filter for joint state/input/parameter estimation

In order to use the pROM within a Kalman Filter scheme, the reduced EOM are transformed from a second order to a first order form via a state space representation [13]. State augmentation is employed for the estimation of the inputs and parameters jointly with the states of the system. The augmented state is defined by extending the regular system states with the unknown quantities as $\mathbf{x}^* = \left[\mathbf{q}^T\ \dot{\mathbf{q}}^T\ \mathbf{u}^{unT}\ \mathbf{p}^T\right]^T \in \mathbb{R}^{2n_{red}+n_{un}+n_p}$. Here the input is split into the unknown inputs $\mathbf{u}^{un} \in \mathbb{R}^{n_{un}}$ and the known inputs $\mathbf{u}^{kn} \in \mathbb{R}^{n_{kn}}$, with a corresponding split in $\mathbf{S}^r$, giving $\mathbf{S}^r_{kn} \in \mathbb{R}^{n_{red}\times n_{kn}}$ and $\mathbf{S}^r_{un} \in \mathbb{R}^{n_{red}\times n_{un}}$.

The time evolution of inputs and parameters is represented using a zeroth order random walk model [10, 13, 12] where each augmented state is considered as constant with the addition of white Gaussian noise:

$$\dot{\mathbf{u}}^{un}(t) = \mathbf{0} + \mathbf{r}_u(t) \tag{18}$$

$$\dot{\mathbf{p}}(t) = \mathbf{0} + \mathbf{r}_p(t) \tag{19}$$

The augmented system can then be represented as:

$$\begin{cases} \dot{\mathbf{x}^*}(t) = \mathbf{A}^*(\mathbf{x}^*)\mathbf{x}^*(t) + \mathbf{B}^*(\mathbf{x}^*)\mathbf{u}^{kn}(t) \\ \mathbf{y}(t) = \mathbf{H}^*(\mathbf{x}^*)\mathbf{x}^*(t) + \mathbf{D}^*(\mathbf{x}^*)\mathbf{u}^{kn}(t) \end{cases} \tag{20}$$

in which the vector $\mathbf{y} \in \mathbb{R}^{n_m}$ contains the outputs from measurements, and the augmented state and input matrices are defined as:

$$\mathbf{A}^*(\mathbf{x}^*) = \begin{bmatrix} \mathbf{0} & \mathbf{I} & \mathbf{0} & \mathbf{0} \\ -\mathbf{M}^{r^{-1}}\mathbf{K}^r & -\mathbf{M}^{r^{-1}}\mathbf{C}^r & \mathbf{M}^{r^{-1}}\mathbf{S}^r_{un} & \mathbf{0} \\ \mathbf{0} & \mathbf{0} & \mathbf{0} & \mathbf{0} \\ \mathbf{0} & \mathbf{0} & \mathbf{0} & \mathbf{0} \end{bmatrix} \tag{21}$$

$$\mathbf{B}^*(\mathbf{x}^*) = \begin{bmatrix} \mathbf{0} \\ \mathbf{M}^{r^{-1}}\mathbf{S}^r_{kn} \\ \mathbf{0} \\ \mathbf{0} \end{bmatrix} \tag{22}$$

The output and feedthrough matrices $\mathbf{H}(\mathbf{p})$ and $\mathbf{D}(\mathbf{p})$ depend on the quantity measured and are explicitly defined in section 4. Note that here and in the following equations the dependency of $\mathbf{K}^r$, $\mathbf{C}^r$ and $\mathbf{M}^r$ on the parameters is not written explicitly, if not needed, for notation clarity.

The augmented model has a nonlinear dependency on the parameters, resulting in general in a nonlinear dependency on the augmented state vector. Because of this, it is necessary to employ a non-linear KF approach. Withouth loss of generality with respect to other non-linear KF approaches, the discrete version of the EKF is employed in this work. The EKF has a similar structure with respect to the one of the linear KF, but uses a system linearization to propagate the state error covariance and calculate the Kalman gain. Given the affine dependency of the reduced system matrices on the parameters employed in the pMOR, the linearized system is expected to be smooth and continuous. The next sections describe the time discretization of the system, the linearization procedure, as well as the EKF algorithm.

3.1. Discretization and Linearization

The augmented state-space model in Equation 20 needs to be discretized in time by choosing an appropriate time integration scheme. This work adopts the method described by Risaliti et al. [15] for the discretization and linearization of the state-space equations, in which the integration scheme of choice is the first order implicit Euler scheme. This choice allows a larger time step size compared to explicit time integrator schemes.

The state evolution in time for a time step h is discretized as:

$$\mathbf{x}^*_k = \mathbf{x}^*_{k-1} + h\dot{\mathbf{x}}^*_k \tag{23}$$

The implicit equation governing the system is then:

$$\mathbf{g}_d(\mathbf{x}^*_{k-1}, \mathbf{x}^*_k, \mathbf{u}^{kn}_k) = \mathbf{x}^*_{k-1} - \mathbf{x}^*_k + h\left(\mathbf{A}^*\left(\mathbf{x}^*_k\right)\mathbf{x}^*_k + \mathbf{B}^*\left(\mathbf{x}^*_k\right)\mathbf{u}^{kn}_k\right) = \mathbf{0} \tag{24}$$

This equation is solved for $\mathbf{x}_k$ in the EKF prediction step to advance the value of the states from $k-1$ to k.

The EKF linearization requires the extraction of the underlying explicit equation associated with Equation 24 as detailed in [15]. This explicit function exists locally if the corresponding implicit function is continuously differentiable. This property is guaranteed by the adopted affine parameter dependency. The underlying explicit function can be found using a Taylor series expansion around the linearization point $[\mathbf{x}_{k-1}^{*,0}\ \mathbf{x}_{k}^{*,0}]$, truncated at the first order:

$$\mathbf{g}_d(\mathbf{x}_{k-1}^*, \mathbf{x}_k^*, \mathbf{u}_k^{kn}) \approx \mathbf{g}_d^0 + \left.\frac{\partial \mathbf{g}_d}{\partial \mathbf{x}_k^*}\right|_0 (\mathbf{x}_k^* - \mathbf{x}_k^{*,0}) + \left.\frac{\partial \mathbf{g}_d}{\partial \mathbf{x}_{k-1}^*}\right|_0 (\mathbf{x}_{k-1}^* - \mathbf{x}_{k-1}^{*,0}) \approx 0 \tag{25}$$

where $\mathbf{g}_d^0 = \mathbf{g}_d(\mathbf{x}_{k-1}^{*,0}, \mathbf{x}_k^{*,0}, \mathbf{u}_k^{kn})$. Furthermore, $\mathbf{x}_k^*$ can be explicitly defined as:

$$\mathbf{f}_d(\mathbf{x}_{k-1}^*, \mathbf{u}_k^{kn}) = \mathbf{x}_k^* = \mathbf{x}_k^{*,0} - \left(\left.\frac{\partial \mathbf{g}_d}{\partial \mathbf{x}_k^*}\right|_0\right)^{-1} \left[\mathbf{g}_d^0 + \left.\frac{\partial \mathbf{g}_d}{\partial \mathbf{x}_{k-1}^*}\right|_0 (\mathbf{x}_{k-1}^* - \mathbf{x}_{k-1}^{*,0})\right] \tag{26}$$

from which the Jacobian matrix is defined as:

$$\mathbf{J} = \frac{\partial \mathbf{f}_d(\mathbf{x}_{k-1}^*, \mathbf{u}_k)}{\partial \mathbf{x}_{k-1}^*} = -\left(\left.\frac{\partial \mathbf{g}_d}{\partial \mathbf{x}_k^*}\right|_0\right)^{-1} \left(\left.\frac{\partial \mathbf{g}_d}{\partial \mathbf{x}_{k-1}^*}\right|_0\right) \tag{27}$$

The two derivatives required for the evaluation of the Jacobian matrix are:

$$\frac{\partial \mathbf{g}_d}{\partial \mathbf{x}_k^*} = -\mathbf{I} + h\left[\frac{\partial \mathbf{A}^*(\mathbf{x}_k^*)}{\partial \mathbf{x}_k^*}\mathbf{x}_k^* + \mathbf{A}^*(\mathbf{x}_k^*)\right] + h\left[\frac{\partial \mathbf{B}^*(\mathbf{x}_k^*)}{\partial \mathbf{x}_k^*}\mathbf{u}_k^{kn}\right] \tag{28}$$

$$\frac{\partial \mathbf{g}_d}{\partial \mathbf{x}_{k-1}^*} = \mathbf{I} \tag{29}$$

The derivatives of the system matrices $\mathbf{A}^*(\mathbf{x}^*)$ and $\mathbf{B}^*(\mathbf{x}^*)$ are straightforward to compute given the affine dependency employed for the pMOR. Given Equation 21 and Equation 22, $\mathbf{A}^*(\mathbf{x}^*)$ and $\mathbf{B}^*(\mathbf{x}^*)$ only depend on $\mathbf{p}$, hence only their derivatives with respect to $\mathbf{p}$ are non-zero. As $\mathbf{A}^*(\mathbf{x}^*)$ and $\mathbf{B}^*(\mathbf{x}^*)$ are the result of the multiplication of the $\mathbf{M}^{r^{-1}}(\mathbf{p})$, $\mathbf{C}^r(\mathbf{p})$ and $\mathbf{K}^r(\mathbf{p})$ matrices, the chain rule for derivation is applied to these terms to obtain the derivatives with respect to $\mathbf{p}$.

The derivative of the stiffness matrix $\mathbf{K}^r(\mathbf{p})$ depends on the type of parameter considered:

$$\frac{\partial \mathbf{K}^r(\mathbf{p})}{\partial E_i} = \mathbf{K}_i^{r\lambda}\frac{\partial \lambda}{\partial E} + \mathbf{K}_i^{r\mu}\frac{\partial \mu}{\partial E} = \mathbf{K}_i^{r\lambda}\frac{\nu}{(1+\nu)(1-2\nu)} + \mathbf{K}_i^{r\mu}\frac{1}{2(1+\nu)} \tag{30}$$

$$\frac{\partial \mathbf{K}^r(\mathbf{p})}{\partial \nu_i} = \mathbf{K}_i^{r\lambda}\frac{\partial \lambda}{\partial \nu} + \mathbf{K}_i^{r\mu}\frac{\partial \mu}{\partial \nu} = \mathbf{K}_i^{r\lambda}\frac{E(1+2\nu^2)}{(1+\nu)^2(1-2\nu)^2} - \mathbf{K}_i^{r\mu}\frac{E}{2(1+\nu)^2} \tag{31}$$

$$\frac{\partial \mathbf{K}^r(\mathbf{p})}{\partial E_j} = \mathbf{K}_j^E \tag{32}$$

The derivative of the inverse mass matrix $\mathbf{M}^{r^{-1}}(\mathbf{p})$ is needed and can be calculated by using the property of inverse matrices derivation:

$$\frac{\partial \mathbf{M}^{r^{-1}}(\mathbf{p})}{\partial \rho_i} = -\mathbf{M}^{r^{-1}}(\mathbf{p})\frac{\partial \mathbf{M}^{r}(\mathbf{p})}{\partial \rho_i}\mathbf{M}^{r^{-1}}(\mathbf{p}) \qquad \frac{\partial \mathbf{M}^{r}(\mathbf{p})}{\partial \rho_i} = \mathbf{M}_i^{r\rho} \tag{33}$$

Given the proportional damping model used, the derivative of $\mathbf{C}^r(\mathbf{p})$ is a linear combination of the two calculated above.

3.2. Augmented Extended Kalman Filter

The discrete system equations of the system considering noise are:

$$\mathbf{g}_d(\mathbf{x}^*_{k-1}, \mathbf{x}^*_k, \mathbf{u}^{kn}_k) = w_k \tag{34}$$

$$\mathbf{y}_k = \mathbf{h}(\mathbf{x}^*_k, \mathbf{u}^{kn}_k) + v_k \tag{35}$$

where w_k and v_k are white uncorrelated Gaussian noise with the corresponding covariance matrices $\mathbf{Q}_k$ and $\mathbf{R}_k$. The output Equation 35 is commonly referred to as the measurement equation in the context of Kalman filtering.

The discrete-time version of the augmented EKF consists of the following steps:

Prediction

$$\mathbf{g}_d(\mathbf{x}^{*+}_{k-1}, \mathbf{x}^{*-}_k, \mathbf{u}^{kn}_k) = 0 \tag{36}$$

$$\mathbf{J}_{k-1} = \left.\frac{\partial \mathbf{f}_d(\mathbf{x}^*_{k-1}, \mathbf{u}^{kn}_k)}{\partial \mathbf{x}^*_{k-1}}\right|_{\mathbf{x}^{*+}_{k-1}, \mathbf{x}^{*-}_k} \tag{37}$$

$$\mathbf{P}^-_k = \mathbf{J}_{k-1}\mathbf{P}^+_{k-1}\mathbf{J}^T_{k-1} + \mathbf{Q}_{k-1} \tag{38}$$

Correction

$$\mathbf{J}_{m,k} = \left.\frac{\partial \mathbf{h}(\mathbf{x}^*_k, \mathbf{u}^{kn}_k)}{\partial \mathbf{x}^*_k}\right|_{\mathbf{x}^{*-}_k} \tag{39}$$

$$\mathbf{K}_k = \mathbf{P}^-_k\mathbf{J}^T_{m,k}(\mathbf{J}_{m.k}\mathbf{P}^-_k\mathbf{J}^T_{m,k} + \mathbf{R}_k)^{-1} \tag{40}$$

$$\mathbf{x}^{*+}_k = \mathbf{x}^{*-}_k + \mathbf{K}_k(\mathbf{y}_k - \mathbf{h}(\mathbf{x}^{*-}_k, \mathbf{u}^{kn}_k)) \tag{41}$$

$$\mathbf{P}^+_k = (\mathbf{I} - \mathbf{K}_k\mathbf{J}_{m,k})\mathbf{P}^-_k(\mathbf{I} - \mathbf{K}_k\mathbf{J}_{m,k})^T + \mathbf{K}_k\mathbf{R}_k\mathbf{K}^T_k \tag{42}$$

In the former equations, $\mathbf{J}_{k-1}$ is the Jacobian of the system calculated on the a-posteriori estimate from the previous step. The linearized form of the measurement equation around the current estimated state is represented by $\mathbf{J}_{m,k}$ The term $\mathbf{K}_k$ is the Kalman gain, and $\mathbf{P}_k$ is the state error covariance matrix.

Of particular importance in the setup of the filter is the choice of the matrices $\mathbf{Q}$ and $\mathbf{R}$, respectively representing the covariance of the states (also referred to as the plant noise covariance matrix) and of the measurements. They are commonly assumed as constant and set by trial and error procedure or by experience. In literature some rules of thumb for the choice have been proposed (e.g. [13]) or schemes to adapt the value in time (e.g. [35, 18, 36]). In particular, in this work the $\mathbf{R}$ matrix is chosen to be a constant diagonal matrix containing the measurement noise covariance taken directly from the used physical sensor data. The plant noise covariance matrix $\mathbf{Q}$ is also assumed to be constant and diagonal, as the noise is considered to be uncorrelated, and can be split to separate the contributions to the different augmented states as:

$$\mathbf{Q} = \begin{bmatrix} \mathbf{Q}_q & \mathbf{0} & \mathbf{0} & \mathbf{0} \\ \mathbf{0} & \mathbf{Q}_{\dot{q}} & \mathbf{0} & \mathbf{0} \\ \mathbf{0} & \mathbf{0} & \mathbf{Q}_u & \mathbf{0} \\ \mathbf{0} & \mathbf{0} & \mathbf{0} & \mathbf{Q}_p \end{bmatrix} \tag{43}$$

Here, $\mathbf{Q}_q$ and $\mathbf{Q}_{\dot{q}}$ represent the uncertainty on the model, while $\mathbf{Q}_u$ and $\mathbf{Q}_p$ represent the uncertainty on the unknown input and parameters, respectively.
The terms of $\mathbf{Q}_u$ are set using the rule of thumb proposed in [13]. For the i-th unknown input u_i, the relative term on the diagonal of $\mathbf{Q}$ is set as:

$$Q_{u_i} = (h\omega_{u_i} a_{u_i})^2 \tag{44}$$

where ω_{u_i} and a_{u_i} are the expected values of frequency and amplitude of the force. As pointed out in [13] and [15], this method aims at keeping the rate of change of the unknown quantity in a range that allows to correctly track its variation while filtering noise. Following this reasoning, $\mathbf{Q}_p$ is also set using the same rule of thumb:

$$Q_{p_i} = (h\delta_{p_i} a_{p_i})^2 \tag{45}$$

In this case a_p is the initial tentative value for the parameter and δ_p is a scaling factor that helps in the setup of the unknown parameter covariance by decoupling it from the absolute value of the parameter itself as well as the integration scheme time step size. In this way, the influence of δ_p on the estimation results can be studied and applied to parameters with different order of magnitudes. The units of δ_p are equivalent to frequency.

The value of δ_p should typically be set to a low value, as the parameter value is usually constant or slowly varying. It should not be set excessively low, as this can slow down the convergence rate to as well as constrain the tracking of any change of the parameter value in time. Given the adopted zeroth order random walk model, a higher augmented state covariance value for the corresponding parameter state allows for a larger change per timestep, lowering the achieved filtering of noise from the estimated augmented states, which is present due to measurement noise propagation in the correction step of the EKF.

4. Observability analysis

In order for the EKF to be able to correctly estimate the unknown quantities of the system, a proper choice of the measurement set is needed [12, 14, 37]. This choice can be made by analyzing the system observability, which depends on the system-measurement combination $(\mathbf{A}^*, \mathbf{H}^*)$.

4.1. Continuous System Linearization

As noted in [12], observability analysis methods are traditionally developed for linear systems, but given the mild non-linearity of structural systems with respect to parameters it is still worth analyzing the properties of the linearized model around representative linearization points. Furthermore, the analysis is done on the time-continuous system for simplicity reasons, but all results translate directly to the discrete case. The continuous linearized model is represented by $\mathbf{J}_c$ and $\mathbf{J}_m$, which are the derivatives of the state and measurement equations of the continuous-time model in Equation 20 respectively, with respect to the system state.

The Jacobian of the continuous state equation is defined as:

$$\mathbf{J}_c = \frac{\partial \dot{\mathbf{x}}^*}{\partial \mathbf{x}^*} = \mathbf{A}^*(\mathbf{x}^*) + \frac{\partial \mathbf{A}^*(\mathbf{x}^*)}{\partial \mathbf{x}^*}\mathbf{x}^* + \frac{\partial \mathbf{B}^*(\mathbf{x}^*)}{\partial \mathbf{x}^*}\mathbf{u}^{kn} = \begin{bmatrix} \mathbf{0} & \mathbf{I} & \mathbf{0} & \mathbf{0} \\ -\mathbf{M}^{r^{-1}}\mathbf{K}^r & -\mathbf{M}^{r^{-1}}\mathbf{C}^r & \mathbf{M}^{r^{-1}}\mathbf{S}^r_{un} & \frac{\partial \ddot{\mathbf{q}}}{\partial \mathbf{p}} \\ \mathbf{0} & \mathbf{0} & \mathbf{0} & \mathbf{0} \\ \mathbf{0} & \mathbf{0} & \mathbf{0} & \mathbf{0} \end{bmatrix} \tag{46}$$

where

$$\frac{\partial \ddot{\mathbf{q}}}{\partial \mathbf{p}} = -\frac{\partial \mathbf{M}^{r^{-1}}\mathbf{K}^r}{\partial \mathbf{p}}\mathbf{q} - \frac{\partial \mathbf{M}^{r^{-1}}\mathbf{C}^r}{\partial \mathbf{p}}\dot{\mathbf{q}} + \frac{\partial \mathbf{M}^{r^{-1}}}{\partial \mathbf{p}}\mathbf{S}^r_{un}\mathbf{u}^{un} + \frac{\partial \mathbf{M}^{r^{-1}}}{\partial \mathbf{p}}\mathbf{S}^r_{kn}\mathbf{u}^{kn} \tag{47}$$

Some of the terms in Equation 46 and Equation 47 become zero for specific choices of parameter types or specific types of input. If only a set of stiffness parameters $\mathbf{p}_s$ is estimated, $\frac{\partial \ddot{\mathbf{q}}}{\partial \mathbf{p}}$ takes the form:

$$\frac{\partial \ddot{\mathbf{q}}}{\partial \mathbf{p}_s} = -\mathbf{M}^{r^{-1}}\frac{\partial \mathbf{K}^r}{\partial \mathbf{p}_s}(\mathbf{q} + \beta\dot{\mathbf{q}}) = -\mathbf{M}^{r^{-1}}\frac{\partial \mathbf{K}^r}{\partial \mathbf{p}_s}\mathbf{K}^{r^{-1}}\left(\mathbf{S}^r_{un}\mathbf{u}^{un} + \mathbf{S}^r_{kn}\mathbf{u}^{kn} - \mathbf{M}^r(\ddot{\mathbf{q}} + \alpha\dot{\mathbf{q}})\right) \tag{48}$$

If only a set of mass parameters $\mathbf{p}_m$ is to be estimated, $\frac{\partial \ddot{\mathbf{q}}}{\partial \mathbf{p}}$ takes the form:

$$\frac{\partial \ddot{\mathbf{q}}}{\partial \mathbf{p}_m} = -\frac{\partial \mathbf{M}^{r^{-1}}}{\partial \mathbf{p}_m}\left(\mathbf{K}^r(\mathbf{q} + \beta\dot{\mathbf{q}}) - \mathbf{S}^r_{kn}\mathbf{u}^{kn} - \mathbf{S}^r_{un}\mathbf{u}^{un}\right) = -\mathbf{M}^{r^{-1}}\frac{\partial \mathbf{M}^r}{\partial \mathbf{p}_m}(\ddot{\mathbf{q}} + \alpha\dot{\mathbf{q}}) \tag{49}$$

For a measurement in which the dependency on states and inputs can be written in the form:

$$\mathbf{h}(\mathbf{x}^*, \mathbf{u}^{kn}) = \mathbf{H}^*(\mathbf{x}^*)\mathbf{x}^* + \mathbf{D}^*(\mathbf{x}^*)\mathbf{u}^{kn} \tag{50}$$

as it is the case in this work and without loss of generality, the Jacobian results in:

$$\mathbf{J}_m = \frac{\partial \mathbf{h}(\mathbf{x}^*, \mathbf{u}^{kn})}{\partial \mathbf{x}^*} = \mathbf{H}^*(\mathbf{x}^*) + \frac{\partial \mathbf{H}^*(\mathbf{x}^*)}{\partial \mathbf{x}^*}\mathbf{x}^* + \frac{\partial \mathbf{D}^*(\mathbf{x}^*)}{\partial \mathbf{x}^*}\mathbf{u}^{kn} \tag{51}$$

The observability analysis requires the explicit definition of equations for the different kinds of measurements. In this work, strain and acceleration measurements are considered:

Strain Measurements

The strain measurement equation can be derived as the spatial derivative of the nodal displacements. Given the element shape functions, the strain measurement equation can then be stated as [15]:

$$\mathbf{h}_s(\mathbf{x}^*, \mathbf{u}^{kn}) = \mathbf{N}_s \mathbf{z} = \mathbf{N}_s \mathbf{\Psi} \mathbf{q} \tag{52}$$

where $\mathbf{N}_s \in \mathbb{R}^{n_{ms} \times n_{dof}}$ is a shape matrix relating the physical DOFs to the measured strain components in the material points of interest and n_{ms} is the number of strain measurements acquired. In this case:

$$\mathbf{H}_s^* = \begin{bmatrix} \mathbf{N}_s \mathbf{\Psi} & \mathbf{0} & \mathbf{0} & \mathbf{0} \end{bmatrix} \qquad \mathbf{D}_s^* = \mathbf{0} \tag{53}$$

and

$$\mathbf{J}_{m,s} = \mathbf{H}_s^* \tag{54}$$

Acceleration Measurements

The acceleration measurement is can be expressed as a linear combination of nodal accelerations, so that:

$$\mathbf{h}_a(\mathbf{x}^*, \mathbf{u}^{kn}) = \mathbf{N}_a \ddot{\mathbf{z}} = \mathbf{N}_a \mathbf{\Psi} \ddot{\mathbf{q}} = \mathbf{N}_a \mathbf{\Psi} \mathbf{M}^{r^{-1}} \left(-\mathbf{C}^r \dot{\mathbf{q}} - \mathbf{K}^r \mathbf{q} + \mathbf{S}_{kn}^r \mathbf{u}^{kn} + \mathbf{S}_{un}^r \mathbf{u}^{un} \right) \tag{55}$$

where $\mathbf{N}_a \in \mathbb{R}^{n_{ma} \times n_{dof}}$ is a shape matrix relating the physical acceleration DOFs to the acceleration of the material points of interest and and n_{ma} is the number of acceleration measurements acquired. In this case:

$$\mathbf{H}_a^*(\mathbf{x}^*) = \mathbf{N}_a \mathbf{\Psi} \begin{bmatrix} -\mathbf{M}^{r^{-1}} \mathbf{K}^r & -\mathbf{M}^{r^{-1}} \mathbf{C}^r & \mathbf{M}^{r^{-1}} \mathbf{S}_{un}^r & \mathbf{0} \end{bmatrix} \tag{56}$$

$$\mathbf{D}_a^*(\mathbf{x}^*) = \mathbf{N}_a \mathbf{\Psi} \begin{bmatrix} \mathbf{M}^{r^{-1}} \mathbf{S}_{kn}^r \end{bmatrix} \tag{57}$$

and, by considering the dependency of the reduced matrices with respect to the augmented states (the parameters in particular)

$$\mathbf{J}_{m,a} = \mathbf{N}_a \mathbf{\Psi} \begin{bmatrix} -\mathbf{M}^{r^{-1}} \mathbf{K}^r & -\mathbf{M}^{r^{-1}} \mathbf{C}^r & \mathbf{M}^{r^{-1}} \mathbf{S}_{un}^r & \frac{\partial \ddot{\mathbf{q}}}{\partial \mathbf{p}} \end{bmatrix} \tag{58}$$

4.2. PBH Test

The Popov-Belevitch-Hautus (PBH) observability test [38, 39] states that a sufficient and necessary condition for the observability of the linearized system is that the matrix

$$\mathbf{PBH} = \begin{bmatrix} \mathbf{I}s - \mathbf{J}_c \\ \mathbf{J}_m \end{bmatrix} \tag{59}$$

is of full rank for every value of $s \in \mathbb{C}$. The matrix $\mathbf{I}s - \mathbf{J}_c$ is guaranteed to be full rank for all values of s but the eigenvalues of $\mathbf{J}_c$, which are the values on which the analysis focuses. In particular, the linearized matrix has a number of zero-valued rows at least equal to the number of augmented states, thus it has the same number of zero eigenvalues. It is for this value of s that the observability is most critical; non-zero eigenvalues, while being unobservable, remain stable and thus the system is at least detectable [14]. The $s = 0$ case will then be analyzed in the rest of this section.

The PBH matrix, for $s = 0$ and using strain and acceleration measurements, can be expressed as:

$$\mathbf{PBH} = \begin{bmatrix} \mathbf{0} & -\mathbf{I} & \mathbf{0} & \mathbf{0} \\ \mathbf{M}^{r^{-1}}\mathbf{K}^r & \mathbf{M}^{r^{-1}}\mathbf{C}^r & -\mathbf{M}^{r^{-1}}\mathbf{S}^r_{un} & -\frac{\partial \ddot{\mathbf{q}}}{\partial \mathbf{p}} \\ \mathbf{0} & \mathbf{0} & \mathbf{0} & \mathbf{0} \\ \mathbf{0} & \mathbf{0} & \mathbf{0} & \mathbf{0} \\ \mathbf{N}_s\mathbf{\Psi} & \mathbf{0} & \mathbf{0} & \mathbf{0} \\ -\mathbf{N}_a\mathbf{\Psi}\mathbf{M}^{r^{-1}}\mathbf{K}^r & -\mathbf{N}_a\mathbf{\Psi}\mathbf{M}^{r^{-1}}\mathbf{C}^r & \mathbf{N}_a\mathbf{\Psi}\mathbf{M}^{r^{-1}}\mathbf{S}^r_{un} & \mathbf{N}_a\mathbf{\Psi}\frac{\partial \ddot{\mathbf{q}}}{\partial \mathbf{p}} \end{bmatrix} \tag{60}$$

Some conclusions can be drawn directly:

- In order to have full observability, a number of strain measurements at least equal to the total number of unknown quantities (inputs and parameters) should be employed. The rows relative to acceleration measurements in Equation 60 are in fact always a linear combination of the second block rows. For any application case then, the use of only acceleration measurements does not allow for an observable system. Acceleration measurements are still important since they add information useful to improve the performances of the estimation procedure

- Parameters related to mass cannot be observed in a static condition (for which $\frac{\partial \ddot{\mathbf{q}}}{\partial \mathbf{p}}$ is zero) because the last block column becomes zero. This follows the practical intuition that in a static case the inertial term is not excited and thus measurements carry no useful information.

Other conclusions can be made in particular cases for which the equations simplify and it is possible to observe linear dependency of the columns of the PBH matrix. In the next subsection the observability for the case of a single parametrized material is discussed.

4.3. Observability Analysis for a Single Material

This section considers the case for which one material is parameterized for both Young's modulus and density. In this case the mass, stiffness and damping matrices assume the simple form:

$$\mathbf{K}^r = E\mathbf{K}^{rE} \tag{61}$$

$$\mathbf{M}^r = \rho\mathbf{M}^{r\rho} \tag{62}$$

$$\mathbf{C}^r = \alpha\rho\mathbf{M}^{r\rho} + \beta E\mathbf{K}^{rE} \tag{63}$$

This simplified case yields the following derivatives:

$$\frac{\partial \ddot{\mathbf{q}}}{\partial E} = -\frac{1}{\rho}\mathbf{M}^{r\rho^{-1}}\mathbf{K}^{rE}\left(\mathbf{q} + \beta\dot{\mathbf{q}}\right) = \frac{1}{\rho E}\mathbf{M}^{r\rho^{-1}}\left(\mathbf{S}^r_{kn}\mathbf{u}^{kn} + \mathbf{S}^r_{un}\mathbf{u}^{un}\right) - \frac{1}{E}(\ddot{\mathbf{q}} + \alpha\dot{\mathbf{q}}) \tag{64}$$

$$\frac{\partial \ddot{\mathbf{q}}}{\partial \rho} = -\frac{E}{\rho^2}\mathbf{M}^{r\rho^{-1}}\left(\mathbf{K}^{rE}\left(\mathbf{q} + \beta\dot{\mathbf{q}}\right) - \mathbf{S}^r_{kn}\mathbf{u}^{kn}\right) = -\frac{1}{\rho}(\ddot{\mathbf{q}} + \alpha\dot{\mathbf{q}}) \tag{65}$$

For $s = 0$, the PBH matrix is:

$$\mathbf{PBH} = \begin{bmatrix} \mathbf{0} & -\mathbf{I} & \mathbf{0} & \mathbf{0} & \mathbf{0} \\ \frac{E}{\rho}\mathbf{M}^{r\rho^{-1}}\mathbf{K}^{rE} & \left(\alpha + \frac{\beta E}{\rho}\mathbf{M}^{r\rho^{-1}}\mathbf{K}^{rE}\right) & -\frac{1}{\rho}\mathbf{M}^{r\rho^{-1}}\mathbf{S}^{r}_{un} & -\frac{\partial \ddot{\mathbf{q}}}{\partial E} & -\frac{\partial \ddot{\mathbf{q}}}{\partial \rho} \\ \mathbf{0} & \mathbf{0} & \mathbf{0} & \mathbf{0} & \mathbf{0} \\ \mathbf{0} & \mathbf{0} & \mathbf{0} & \mathbf{0} & \mathbf{0} \\ \mathbf{0} & \mathbf{0} & \mathbf{0} & \mathbf{0} & \mathbf{0} \\ \mathbf{N}_s\mathbf{\Psi} & \mathbf{0} & \mathbf{0} & \mathbf{0} & \mathbf{0} \\ -\mathbf{N}_a\mathbf{\Psi}\frac{E}{\rho}\mathbf{M}^{r\rho^{-1}}\mathbf{K}^{rE} & -\mathbf{N}_a\mathbf{\Psi}\left(\alpha + \frac{\beta E}{\rho}\mathbf{M}^{r\rho^{-1}}\mathbf{K}^{rE}\right) & \mathbf{N}_a\mathbf{\Psi}\frac{1}{\rho}\mathbf{M}^{r\rho^{-1}}\mathbf{S}^{r}_{un} & \mathbf{N}_a\mathbf{\Psi}\frac{\partial \ddot{\mathbf{q}}}{\partial E} & \mathbf{N}_a\mathbf{\Psi}\frac{\partial \ddot{\mathbf{q}}}{\partial \rho} \end{bmatrix} \tag{66}$$

It can be observed that:

- Given Equation 64 and Equation 65, it is impossible to simultaneously estimate E and ρ if there is no input being applied to the system. This implies that under a free response condition the effect of mass and inertia is not distinguishable. The last two columns become in fact linearly dependent.
- It is impossible to simultaneously estimate inputs, E, ρ if there is not at least one non-zero known input.
- If E and the input are to be estimated, the system is not observable in static conditions. This implies that it is impossible to estimate both the Young's modulus and a static load, confirming the intuition that the system inversion in this case is not feasible.

5. Numerical Validation

This section presents a numerical validation of the main methodology proposed and presented in the previous chapters, i.e. the joint state/input/parameter estimation, using the blade FE model introduced in subsection 2.3. In a first part an Optimal Sensor Placement (OSP) procedure is employed to select the sensors to use for the estimation. Then a setup of the filter is executed using numerical data. The robustness and effectiveness of the chosen setup is numerically validated.

5.1. Sensor Selection

The physical blade is instrumented with strain and acceleration sensors spread over its entire length, as shown in Figure 7, therefore also virtual sensors are placed at the same locations. In particular, the sensors used are:

- 10 rectangular strain gage rosettes placed symmetrically on the top and bottom face at 5 different sections along the length of the blade (numbered from 0 to 4 in the remaining part of the paper).
- 4 uniaxial strain gages placed symmetrically on the top and bottom face of sections 2 and 3 along the axis of the blade.

- 10 triaxial accelerometers placed on the top face at 8 sections along the length of the blade (named from A to H in the remaining part of the paper). Their axes are aligned with the global ones.

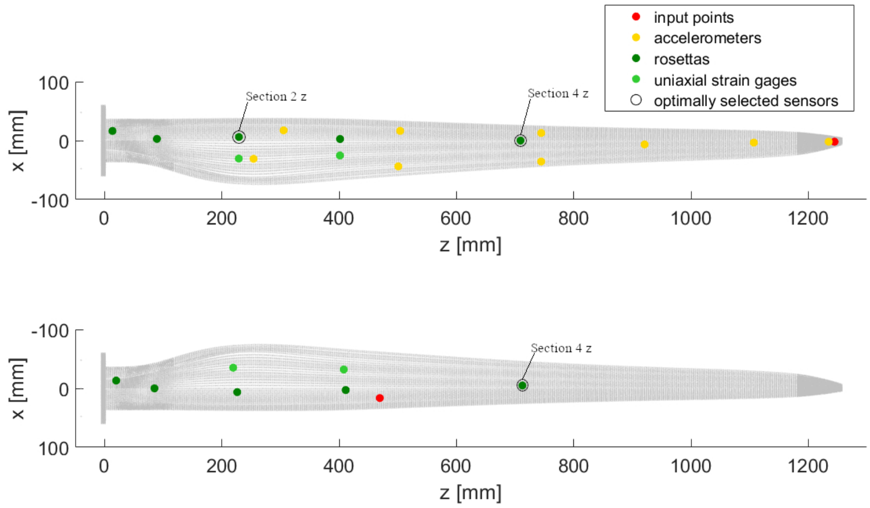

Figure 7: Position of sensors and input points on the blade. The 3 sensors labeled are the rosettes of which the z sensors were selected by the OSP procedure.

Only a subset of sensors is used for the estimation, while the remaining ones are used for validation purposes: the estimated values are compared with the simulated ones, for the numerical applications, or with the measured ones, for experimental applications. A minimal number of strain gages is required for observability reasons, as discussed in section 4. The addition of accelerometers to this set could extend the overall bandwidth of the filter. The frequency range investigated in this work is however low enough to allow the use of only strain gages for the estimation, while the accelerations sensors will therefore be used for validation.

The selection of strain gages to use for the estimation has been based on the OSP strategy described in [37]. There the aim is to find the optimal location and orientation of sensors in order to guarantee the best observability for unknown inputs. The strategy starts by screening an initial sensor pool spread over the entire surface of the model, and then subsequently removing the sensors that contribute the least to the observability metric of interest. For the blade setup considered in this work, the OSP strategy has been adapted to start from the pool of existing sensors, following the subsequent steps as discussed in the reference.

The OSP procedure has been used to select a set of 3 strain gages, since that is the minimum required number for estimation of the two parameters and one input. The selected sensors are the ones oriented along the axis of the blade in the rosettes on the top face of sections 2 and 4 and on the bottom face of section 4, as shown on Figure 7. The OSP approach targets input estimation and therefore it is only used in this work as a way to select the sensors to use, without any claim of global optimality. The extension of the OSP procedure to consider also observability of parameters is out of the scope of this work and is therefore not explored here.

5.2. Filter Setup

In the case of experimental data, the measurement noise covariance matrix $\mathbf{R}$ is set using values extracted for each physical sensor. If numerical measurements are used, the noise level is known and its covariance value can be directly used as the diagonal entries of $\mathbf{R}$. The initial value for $\mathbf{P}$ is set by assuming a low initial error on the states and an initial error on the parameters in the same order of magnitude as the expected parameter values themselves to improve initial convergence.

It is common practice for AKF application to set the covariance of the plant to a low value to let the filter follow the numerical model predictions [13, 12]. In the following application $\mathbf{Q}_q = \epsilon\mathbf{I}$ and $\mathbf{Q}_{\dot{q}} = \epsilon\mathbf{I}$, where ϵ represents the machine precision.

Setting the zeroth order random walk noise covariance to a low value implies that the associated augmented state is expected to remain constant or vary slowly. A large value permits a large variation of the associated augmented state during each time step. These covariance values depend on the assumed nature of the augmented states, i.e. having a specific expected quasi-static or dynamic behavior. In the remaining part of this section the effect of choosing different augmented state noise covariance values on the corresponding estimation results is shown. The values are represented by ω_u or δ_p, which are used to calculate the covariance values by applying Equation 44 or Equation 45. The following estimation cases are based on numerical data in order to have full control and assure that any variations in the estimated values are only due to the noise present in the supplied numerical measurements. The measurements are generated by a forward simulation using the same integration scheme as in subsection 2.3 and then zero-mean white Gaussian noise is added. A 20 Hz sinusoidal load (Figure 8) is used for this analysis, without loss of generality.

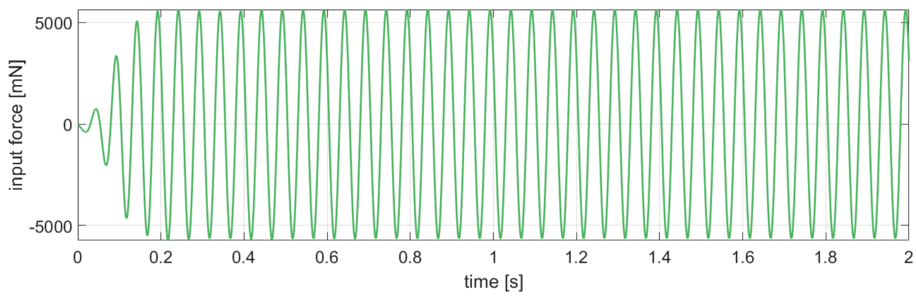

Figure 8: 20Hz sine input

The first case considered is the estimation of a constant Young's modulus. The estimated parameter value for different values of δ_E is shown in Figure 9. In order to evaluate the estimation performance, the average error is considered along with the maximum and minimum error that define the interval in which the estimated parameter evolves. Ideally the average value for the error should be close to zero and the maximum and minimum interval should be as narrow as possible. A large interval indicates a large variation usually caused by noise. The desired behavior of the filter in this first case is that the estimated parameter value converges and stays as constant as possible. All the δ_E values allow for similar convergence behavior, with a similar and small average error in the last part. It can also be seen that the evolution interval is narrow for δ_E values below a certain threshold ($10^{-2}Hz$) while for higher values it increases, showing more measurement noise leaking into the estimate, as explained in subsection 3.2. It can be concluded in this case that a covariance value as low as possible is desired, and that any value below a certain threshold will allow for good results.

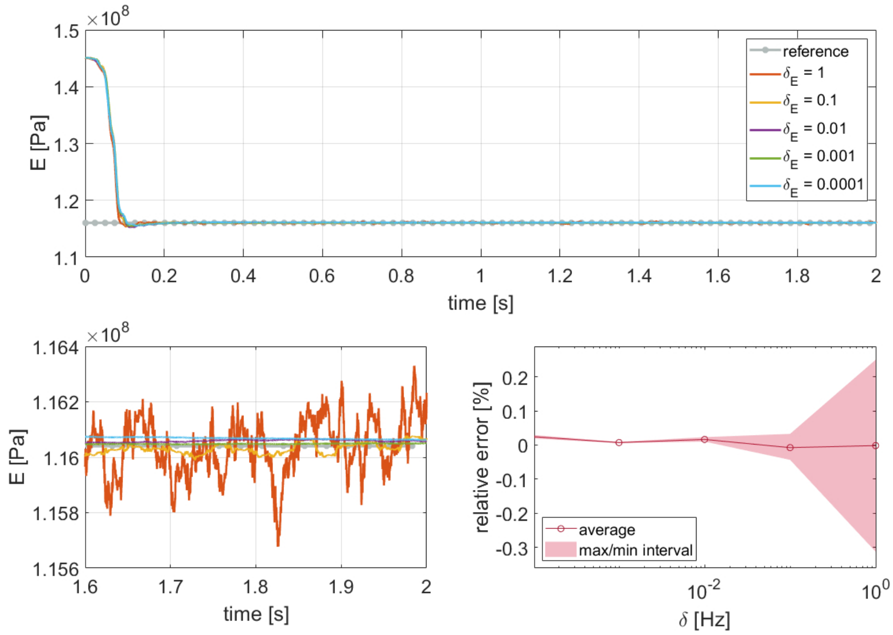

Figure 9: Estimated value of E with numerical data for sine load with different values of δ_E. A zoom on the last 0.4s is presented together with the estimation error on the same time interval.

A second case is considered where the parameter is degrading in time (Figure 10). A low δ_E value constrains the rate of change of the parameter, preventing it from properly tracking the real value. The minimum δ_E value that allows to properly track the evolution of the parameter for the presented case is $1Hz$. By further increasing the δ_E value, the average error remains small, while the variation interval gets larger, showing that more measurement noise leaks into the estimated augmented states. In this case a larger δ_E value should be used.

These results indicate that there is no overall optimal covariance value setting and the setting thus has to be made according to the application case and the expected evolution of the augmented state over time. A representative virtual exercise could be carried out to select these settings. In a system identification case, where the model parameters are expected to be constant, δ_E can be set as low as possible. If an abrupt change in parameter values is expected instead, a high value should to be employed at the expense of a more noisy estimate (as explained in subsection 3.2).

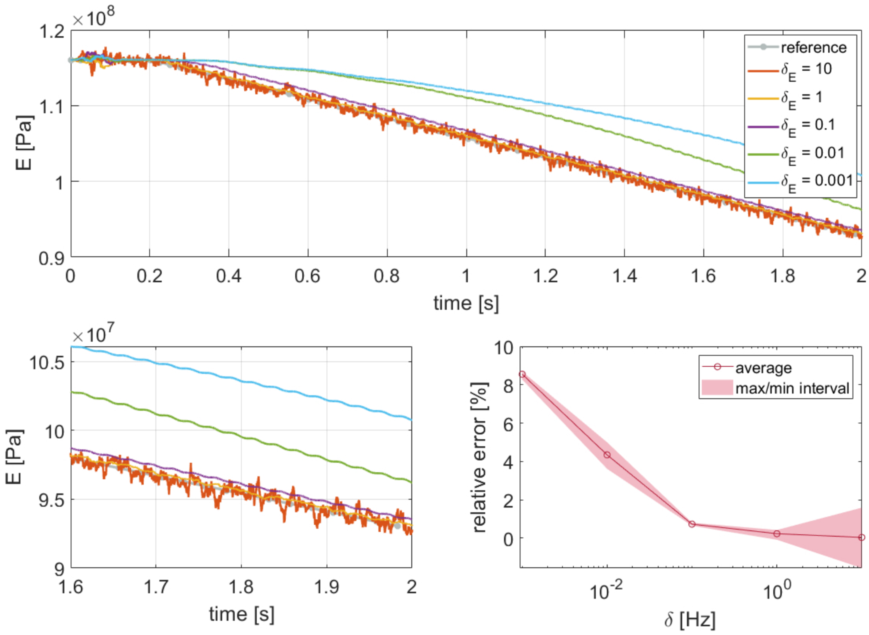

Figure 10: Estimated value of degrading E with numerical data for sine load with different values of δ_E. A zoom on the last 0.4s is presented together with the estimation error on the same time interval.

A third case is considered where E and ρ are estimated simultaneously, as shown in Figure 11. If the covariance values are not high enough, the estimated parameters tend to converge much slower as compared to the single parameter case. Also here a covariance value for which the average error stabilizes corresponds to $1Hz$. The decreased convergence rate can be explained by the fact that the dynamic stiffness of a linear structural system tends to depend on the ratio between stiffness and mass parameters. Once the filter has reached the correct stiffness/mass ratio (by means of the estimated parameters), the dynamic response of the system using these estimated parameter values is close to the real response, causing the low convergence rate that thus has to be compensated for with higher covariance values of the parameters. This is shown in Figure 12. Here, the ratio of the two parameters converges faster than their single values.

When parameters and input are estimated simultaneously, their covariance settings appears to be uncoupled for this specific application, since they only effect their relative augmented state's convergence. As a consequence, the choice of covariance values for parameters, as discussed above, also applies for this case. The results shown in Figure 13 are calculated for a fixed $\delta_E = 10^{-3}$ and varying ω_u. As discussed and shown in [12, 40, 41], a small lag is usually present in the estimated input with respect to the measured one, even when the amplitude is correctly estimated. This lag can also be clearly seen in the results of this application when the frequency of the input is set to the known value of 20Hz. This represents a mismatch in the case of input only estimation. When parameters are jointly estimated with the inputs, this phase shift is compensated for by the filter through an estimated parameter value different from the real one. Increasing the estimated input frequency value reduces the observed lag at the expense of more

579 noise. This in turn reduces the error on the parameter estimation, as can be clearly seen
580 in the plot of parameter error with respect to ω_u.

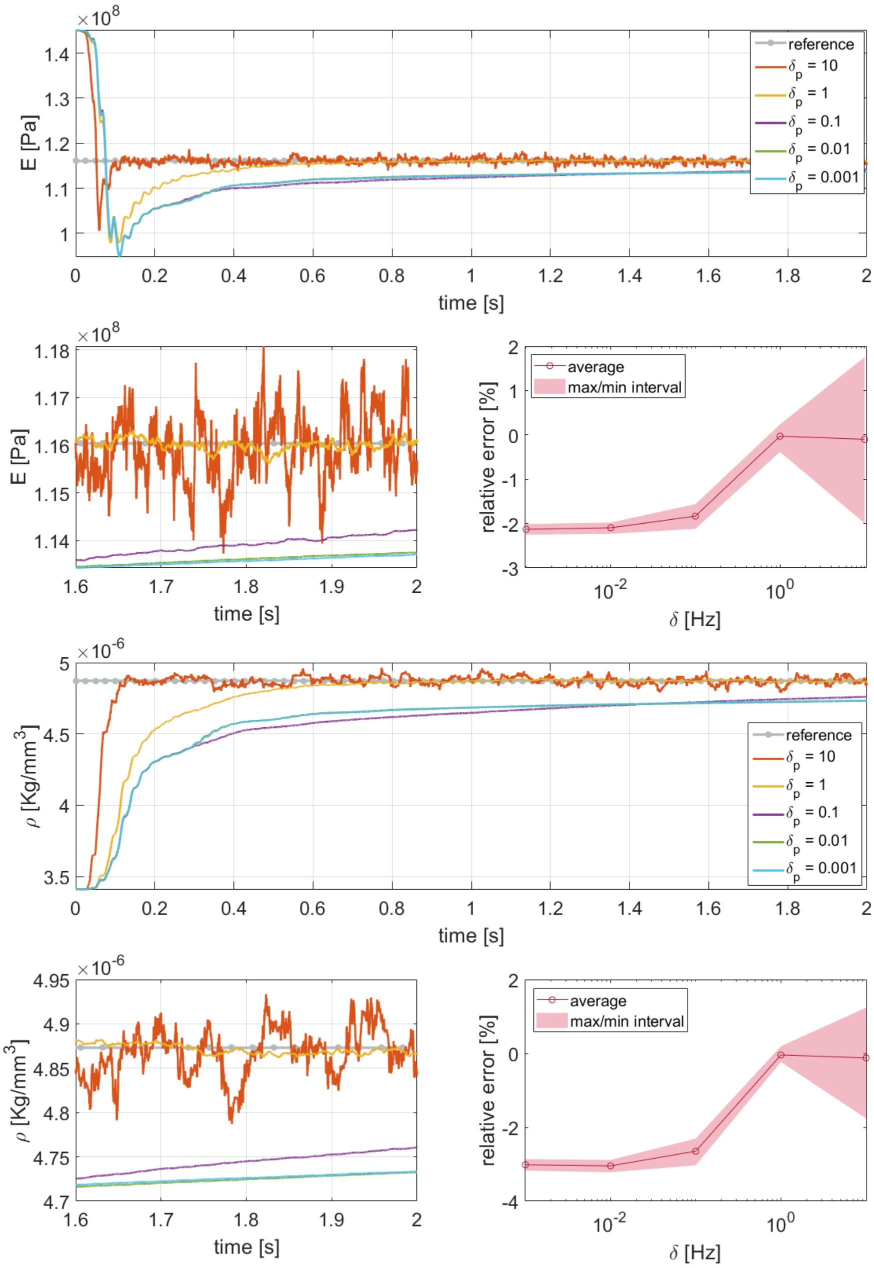

Figure 11: Estimated values of E and ρ with numerical data for sine load with different values of $\delta_p = \delta_E = \delta_\rho$. A zoom on the last 0.4s is presented together with the estimation error on the same time interval.

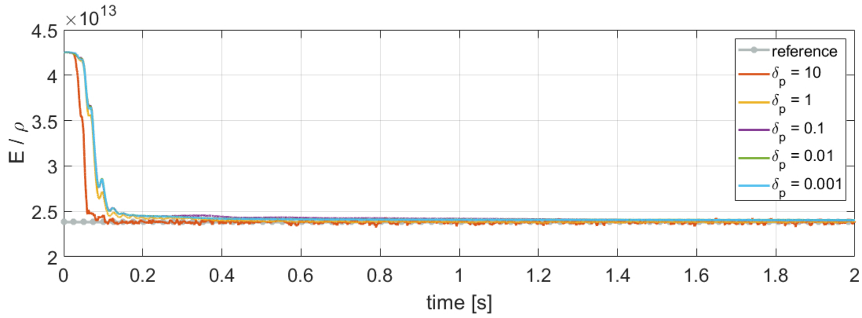

Figure 12: Value of the ratio between estimated E and ρ for the case shown in Figure 11.

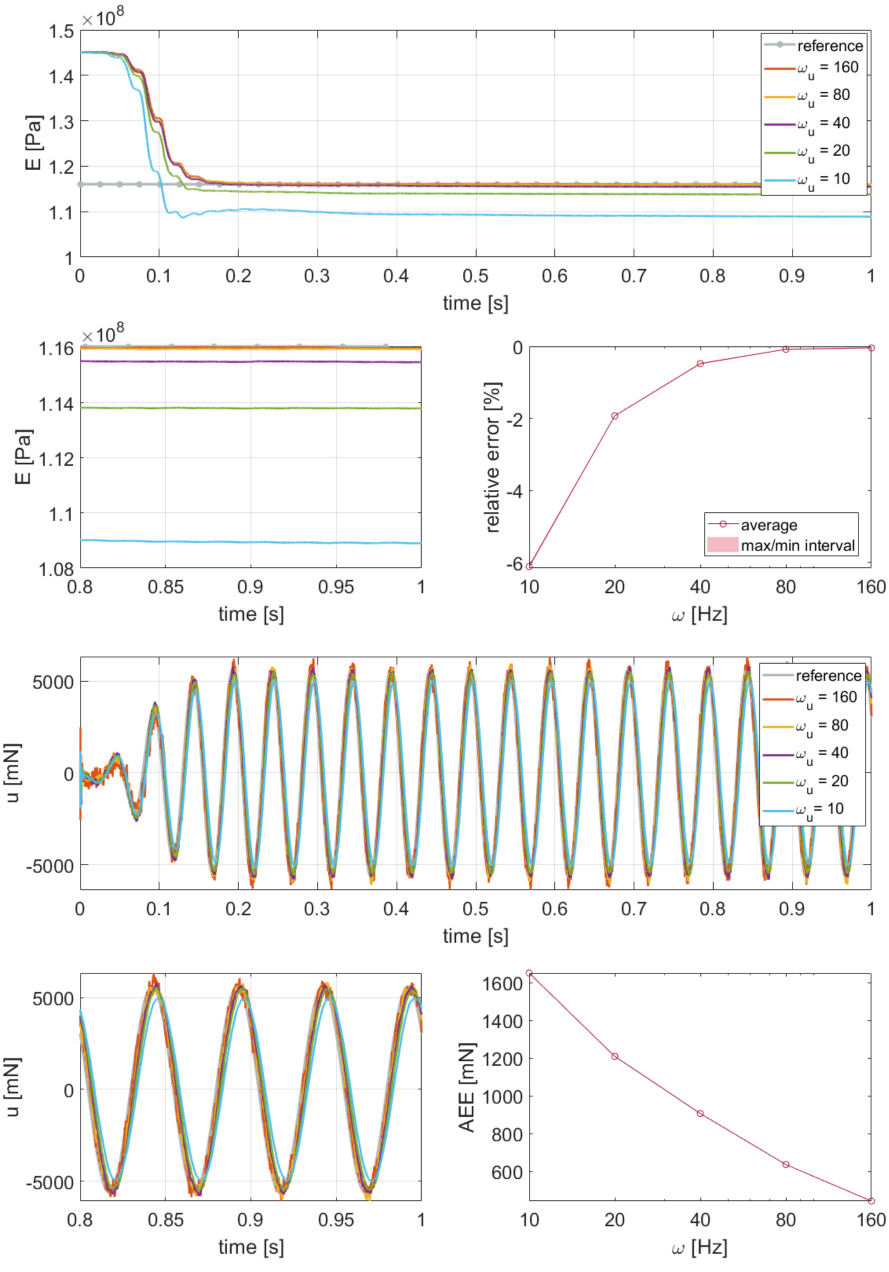

Figure 13: Estimated values of E and inputs with numerical data for sine load with different values of ω_u and $\delta_E = 10^{-3} Hz$. A zoom on the last 0.2s is presented together with the estimation error on the same time interval.

581 *5.3. Numerical Estimation Validation*

582 A first validation of the estimation procedure is done using numerical data. This
583 allows, by having full control over the system and the measured data, to asses the per-

formance of the filter with the setup defined in the previous section. The numerical approach also allows to consider the case of a parameter degrading with time, for which no experimental data is available.

As the full set of sensors is estimated, the sensors not used as measurements can be compared with their reference simulation values to assess if the filter can correctly estimate the full field of strains and accelerations by using only a limited set of sensors. This evaluation is based on the Averaged Absolute Error (AAE) metric defined in [15] as $\sum_{i=1}^{T} |y_{est,i} - y_{meas,i}|/T$ where $y_{est,i}$ and $y_{meas,i}$ are the estimated and measured signals at the i-th time step, respectively, and T is the number of steps in the considered time interval. This metric is compared with the Maximum Response Amplitude (MRA) for each case in order to compare the average error with the maximum value assumed by the signal. For this numerical application, the sensor estimation results are shown only for the most complex case of parameter and input estimation, as all the others are comparable.

The inputs used for this validation are a static load on the tip, a 20 Hz sinusoidal load (Figure 8) and a broadband continuous random signal (Figure 14). Data on the inputs is listed in Table 2.

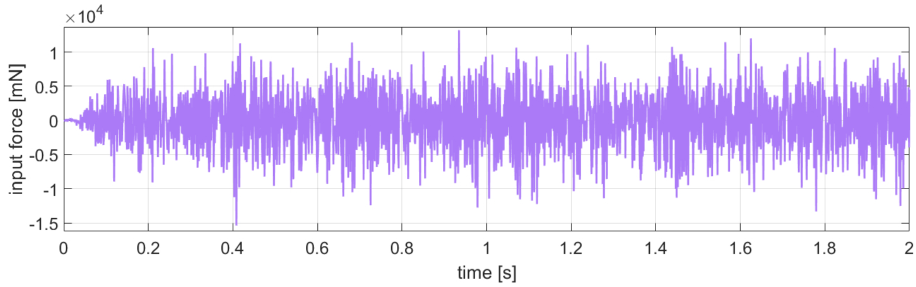

Figure 14: Continuous random input

Table 2: Load case data

Signal type	Frequency	Amplitude
Static	0 Hz	14.7 N
Sine	20 Hz	5 N
Random	0-500 Hz	14 N (max)

Each application case has been run for every possible load case. In some of the cases the static load has not been used since it makes the system unobservable, as shown in the theoretical observability analysis (section 4). White noise, with an amplitude in the order of $10^{-7} m/m$ and $10^{-3} m/s^2$ for strain and acceleration measurements respectively, is added to the generated numerical measurements. Both simulations and estimations use a time step of $0.1ms$.

An overview of the performance of all the cases in terms of parameter estimation is shown in Table 3. This table shows the minimum, maximum and average relative error of the estimated parameters with respect to the reference values in the last 20% of the time interval, for which the estimated values have typically converged to stable values. Analysis of this interval gives an idea on the convergence to the correct value and how much the parameter varies in time after converging.

Table 3: Errors on estimated parameters in last 20% of time interval for numerical measurements

Unknown quantities	**Load**	**Error** [%]			
		Parameter	**min**	**avg**	**max**
E	static	E	0.01	0.01	0.01
	sine	E	0.01	0.02	0.02
	random	E	-0.02	-0.02	-0.02
E, ρ	static	unobservable			
	sine	E	-0.50	-0.22	0.00
		ρ	-0.30	-0.09	0.15
	random	E	-0.23	-0.08	0.16
		ρ	-0.29	-0.07	0.19
degrading E	static	E	-0.06	0.07	0.19
	sine	E	-0.08	0.24	0.43
	random	E	-0.04	0.16	0.38
E, input	static	unobservable			
	sine	E	-0.09	-0.08	-0.07
	random	E	0.18	0.21	0.23
degrading E, input	static	unobservable			
	sine	E	0.07	0.39	0.75
	random	E	0.27	0.56	0.97

5.3.1. Constant Parameter Estimation

As a first application case, the Young's modulus is estimated. The density and the loads are known. The initial value of the augmented state related to the parameter is set to a value 25% higher than the reference value, and its covariance is calculated by setting $\delta_E = 10^{-3} Hz$. This parameter is observable for all considered load cases.

The evolution of the estimated parameter value over a $1s$ time interval is shown in Figure 15. For the static load case the estimated parameter shows a fast convergence to the reference value since the load is applied from the start. For the dynamic cases instead the value converges gradually to the correct one, since the initial input is zero and it gradually increases, allowing the filter to smoothly correct the value of E.

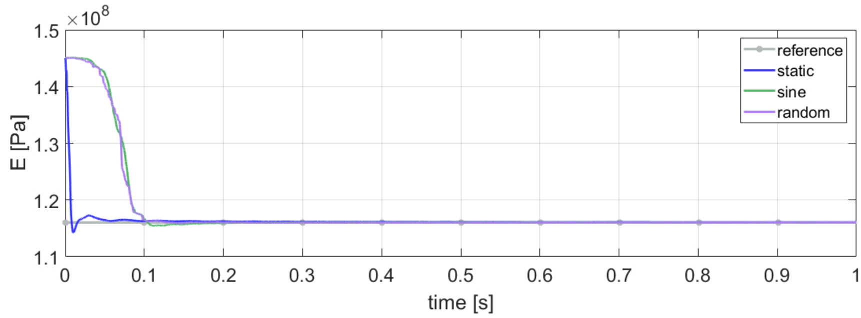

Figure 15: Estimated value of E with numerical data, for all load cases, with $\delta_E = 10^{-3} Hz$.

As a second application case, both Young's modulus and density are unknown. The results are shown in Figure 16. Only the dynamic load cases can be considered, since the density is unobservable for a static input. The initial errors on the augmented states related to E and ρ are respectively set at 25% and -30%. The observed convergence rate is slower and thus a larger δ_p of $1Hz$ is adopted. The converged parameter values estimated by the filter accurately match the reference ones.

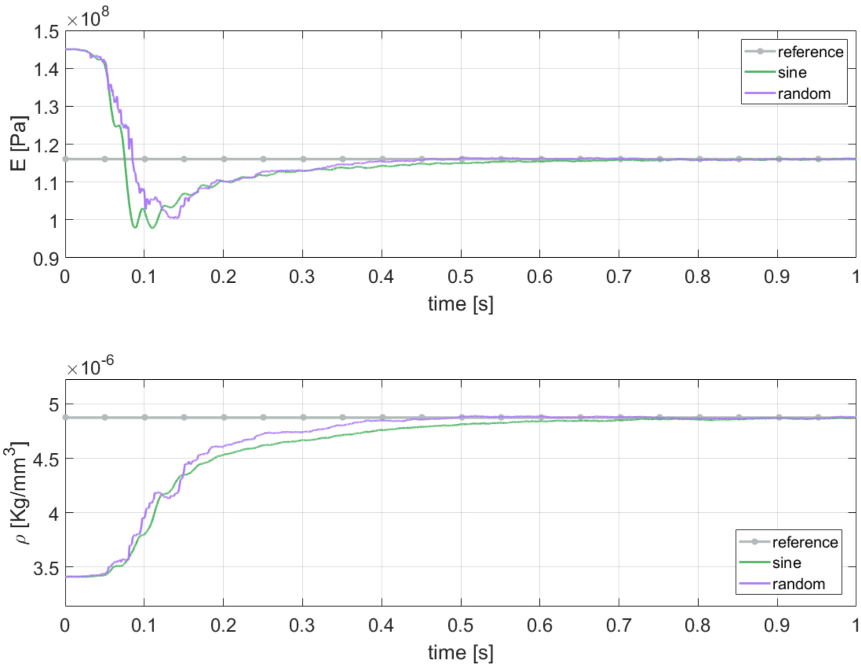

Figure 16: Estimated values of E and ρ with numerical data, for sine and random loads, with $\delta_E = 1Hz$, $\delta_\rho = 1Hz$.

5.3.2. Degrading Parameter Estimation

A fundamental application of the presented methodology is the tracking of a parameter that deteriorates in time. In order to generate numerical data for the deterioration case, a simulation is run using the pROM during which the Young's modulus, starting from the correct value, decreases at a rate of 10%/s. It should be noticed how this type of simulation during which the parameters vary continuously is enabled by the use of the pROM, as it allows to update the model in an efficient way (i.e. without having to recreate the ROM).

The results of the estimation of only E, with $\delta_E = 1Hz$, are shown in Figure 17. The large covariance value needed to allow the correct tracking of the parameter variation causes measurement noise to propagate to the estimated parameter. This can be seen as an acceptable solution as the average error remains small.

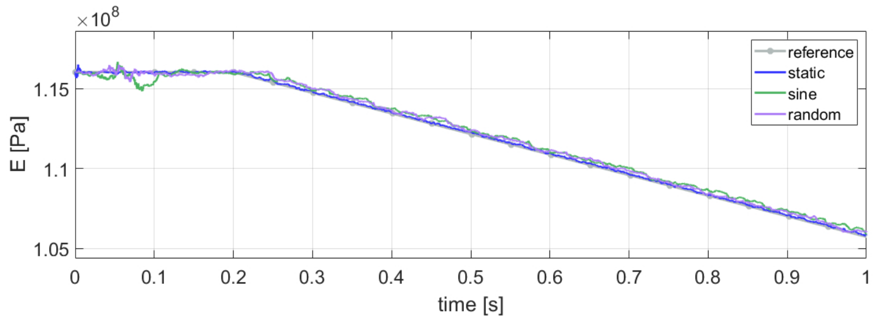

Figure 17: Estimated value of degrading E with numerical data, for all load cases, with $\delta_E = 1Hz$.

5.3.3. Parameter and Input Estimation

As a more complex application case, both the Young's modulus and the input are considered as unknown. In this case the filter has to be able to discern between the influence of a change of parameter values from a time-varying input. The results of the coupled estimation of constant E ($\delta_E = 10^{-3}Hz$) and a dynamic load ($\omega_{u,2} = 80Hz$, $\omega_{u,3} = 2000Hz$) are shown in Figure 18. The system is unobservable for the static load case. Both dynamic load cases show excellent results with a correct and fast estimation of the parameters. The estimated input displays some noise given by the necessity for larger related covariance values, as explained in subsection 5.2, to avoid lag. The estimated sensor errors for both strain sensors and accelerometers are shown in Figure 19. It can be observed how the AAE is always at least one order of magnitude lower that the MRA. Some exceptions are in the accelerometers with lower MRA, due to accelerations being more sensitive to the noise introduced by the input estimation. The estimation procedure also shows good results for the case where the Young's modulus is varying in time, with an unknown input and known density. The results are shown in Figure 20. Here, δ_E is set to 1 Hz and thus more noise is added.

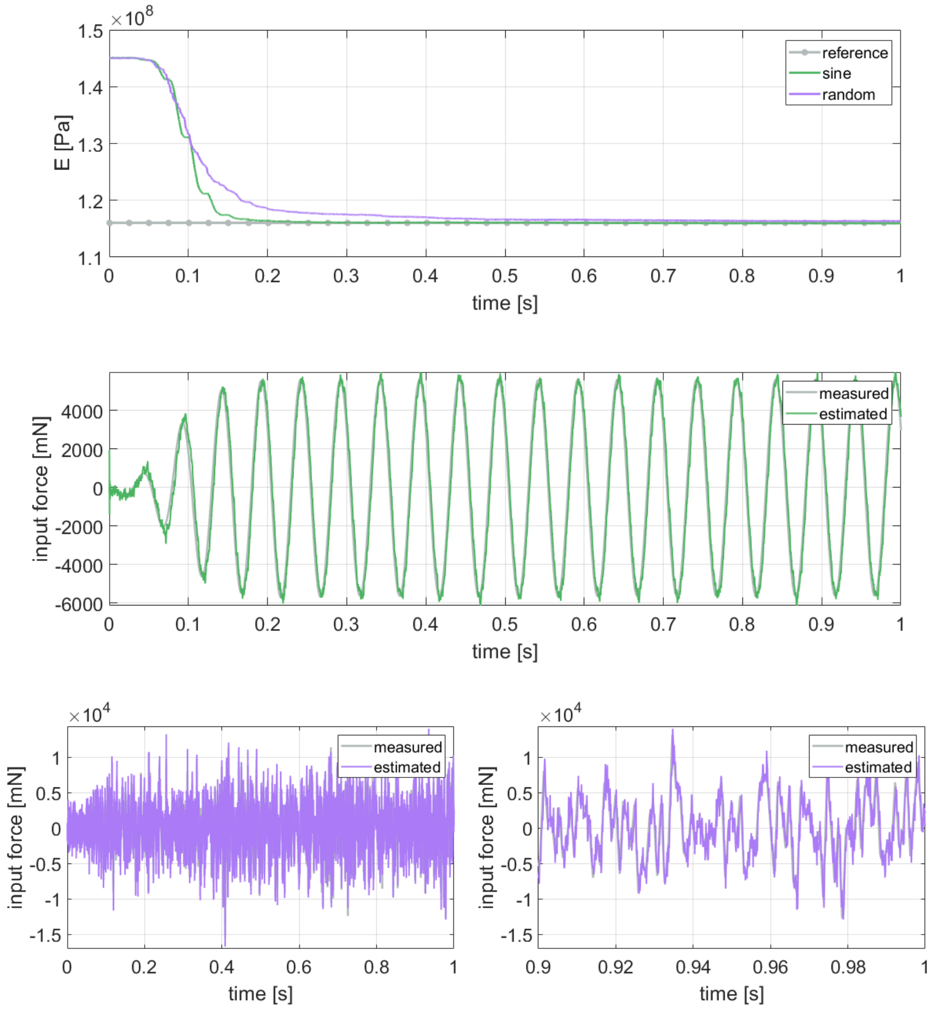

Figure 18: Estimated values of E and inputs with numerical data, for the sine and random load cases, with $\delta_E = 10^{-3}Hz$, $\omega_{u,2} = 80Hz$ and $\omega_{u,3} = 2000Hz$. The right figures show a zoom of the 0.9s to 1s range.

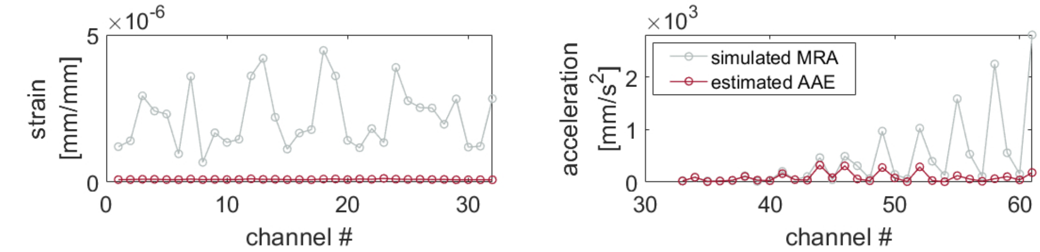

(a) Sine load case

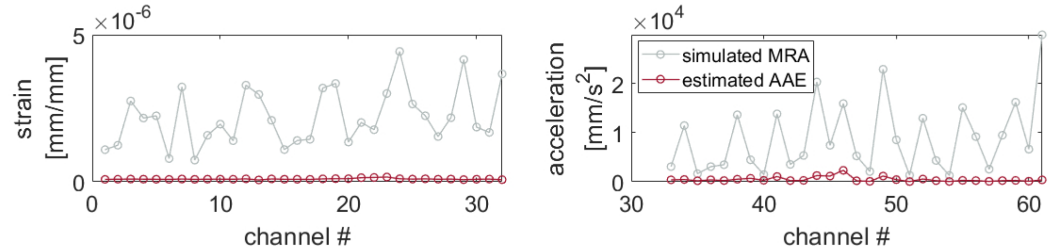

(b) Random load case

Figure 19: Estimated sensors error for the case shown in Figure 18.

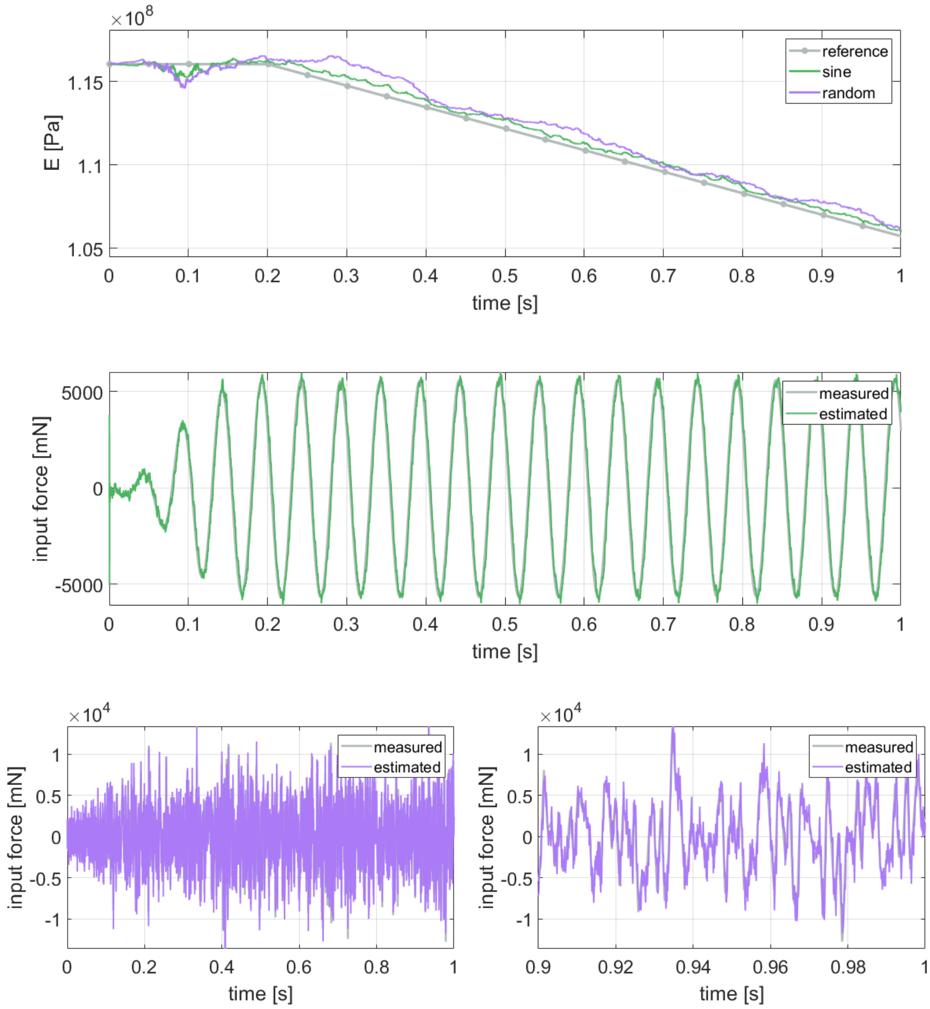

Figure 20: Estimated value of degrading E and input with numerical data, for the sine and random load cases, with $\delta_E = 1Hz$, $\omega_{u,2} = 80Hz$ and $\omega_{u,3} = 2000Hz$. The right figures show a zoom of the 0.9s to 1s range.

5.3.4. Parameter and input estimation with non-zero initial conditions

The former results have been obtained with measurements on a model starting at zero initial conditions. In order to demonstrate the robustness of the filter, input and constant Young's modulus are estimated based on a set of measurements with non-zero initial conditions. This is obtained by simulating the system for 2s and discarding the interval from the start up to 1s. The results of the coupled estimation, with the same setting as in the former section, are shown in Figure 21. The estimated values show an excellent convergence to the reference ones. The main difference with respect to former cases is in the initial steps, where a less gradual convergence behavior is observed. This can be explained by the fact that the filter is setup with different initial conditions, resulting in a larger initial mismatch that is compensated with quick variations of estimated quantities.

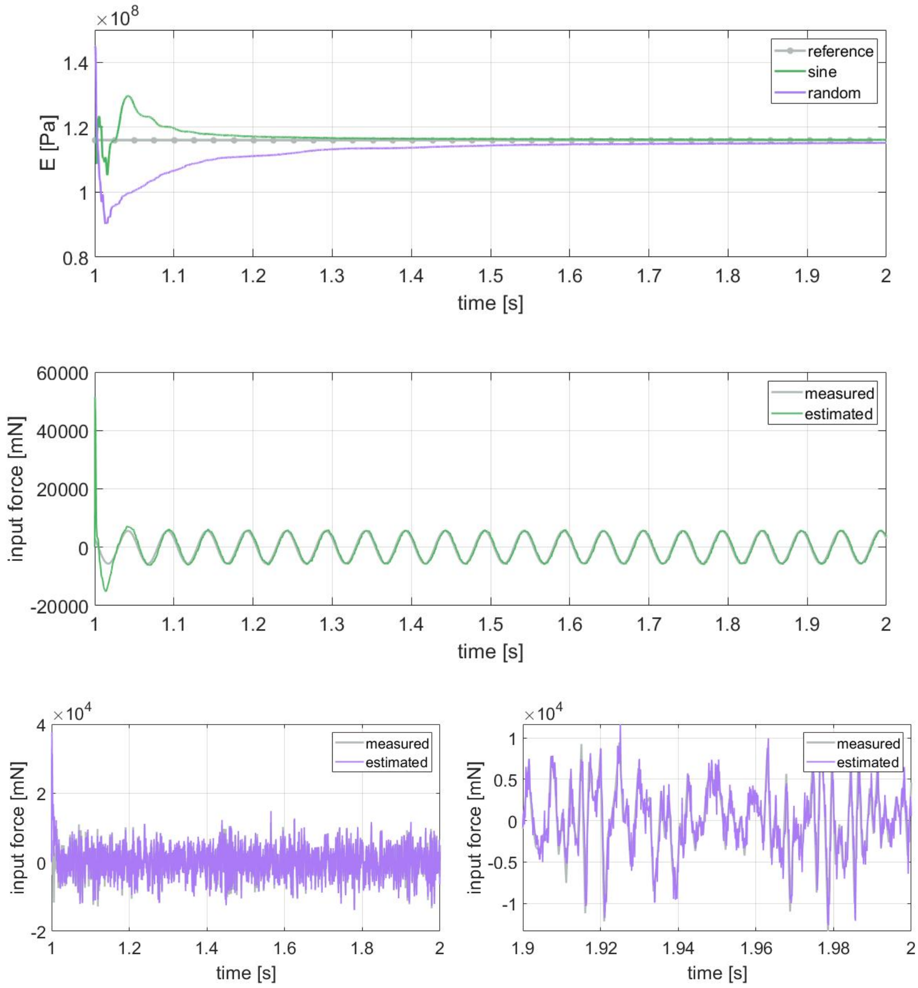

Figure 21: Estimated values of E and inputs with numerical data and non-zero initial conditions, for the sine and random load cases, with $\delta_E = 10^{-3} Hz$, $\omega_{u,2} = 80Hz$ and $\omega_{u,3} = 2000Hz$. The right figures show a zoom of the 1.9s to 2s range.

6. Experimental Validation

In this section, the experimental setup (Figure 22) is presented and the estimation methodology is validated using experimental data.

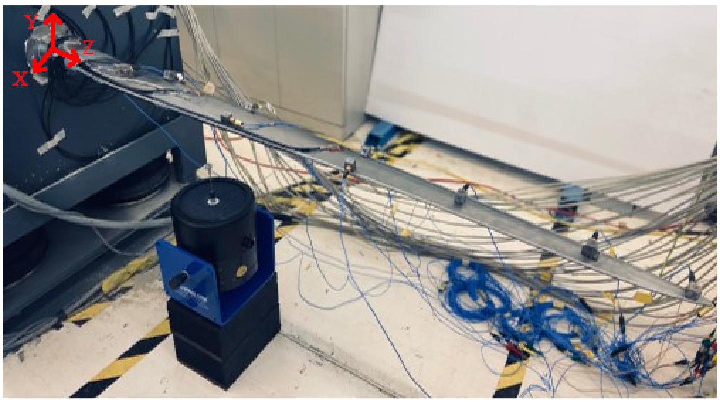

Figure 22: Instrumented blade

The main parameters of the FE model (Figure 2a) representing the physical blade, namely Young's modulus, Poisson's ratio, density and stiffness of the bolts, have been identified by a modal testing procedure and model updating [42] using a commercial FE pre- and post-processing software package [32]. The identified parameter values are listed in Table 4. The damping parameters for the proportional Rayleigh model have been identified using an optimization procedure aimed at finding the values that minimize the error between the experimental and numerical FRFs for one input point (the shaker's application point) and two representative outputs (accelerometers on sections D and H in the global y direction). The identification has been carried out in the 0-50Hz range.

Table 4: Experimentally identified model parameters

E $[GPa]$	ρ $[Kg/m^3]$	ν	α	β	K $[N/mm]$
116.04	4873	0.34208	0.02	0.0005	33167.2

A zero-input acquisition has been done in order to measure the noise level for every sensor. The strain gages and accelerometers as used for data acquisition have noise levels in the order of $10^{-7}m/m$ and $10^{-3}m/s^2$, respectively.

The measurement campaign consisted of separately applying static and dynamic loads to the blade and acquiring data to be used for the estimation. A static load has been applied at the blade tip by suspending a mass of known value $m_s = 1.5Kg$. A 20Hz sine load, following the one as used for the numerical validation, has been applied on a point at the middle of the bottom face of the blade by means of an electrodynamic modal shaker. The tip of the shaker was connected to the blade via a mechanical impedance sensor to measure the applied force.

The measurements have been acquired using a sampling period of $1ms$. Since the estimator uses a time step of $0.1ms$, these are linearly interpolated between sampling points in order to match the filter's time step. An overview of the relative errors for the parameter and input estimation using experimental data is shown in Table 5 for the different considered load cases. The observed errors are small for most cases, with larger variation ranges when compared with the numerical application cases. The different cases are further discussed below. For each of them, the filter has been setup as described in subsection 5.2.

Table 5: Errors on estimated parameters in the last 20% of the considered time interval for experimental measurements

Unknown quantities	**Load**	**Error** [%]			
		Parameter	**min**	**avg**	**max**
E	static	E	0.03	0.04	0.06
	sine	E	1.95	2.00	2.05
E, ρ	static	unobservable			
	sine	E	2.09	3.45	5.01
		ρ	-2.38	-1.00	-0.08
E, input	static	unobservable			
	sine	E	0.46	0.52	0.63

6.1. Parameter Estimation

6.1.1. Young's modulus

For the case where the Young's modulus is estimated, with a known density and input, the augmented state covariance value is calculated by choosing $\delta_E = 10^{-3}Hz$. The observed error is close to zero for the static load input and 2% on average for the sine load case. The results are shown in Figure 23. The values of the estimated sensors as compared to the measured experimental values display a small error, as shown in Figure 24. The main mismatch is present for the sensors mounted closer to the root of the blade, where it is assumed that the boundary conditions have a larger influence on the system dynamics and that the error can thus be attributed to the unmodeled system dynamics related to these boundary conditions. Figure 24 includes also the AAE of the simulated measurements generated through a forward simulation with the reference parameter value. These show a similar behavior to estimated ones, proving that the error is not introduced by the filter but it is due to a mismatch in the model.

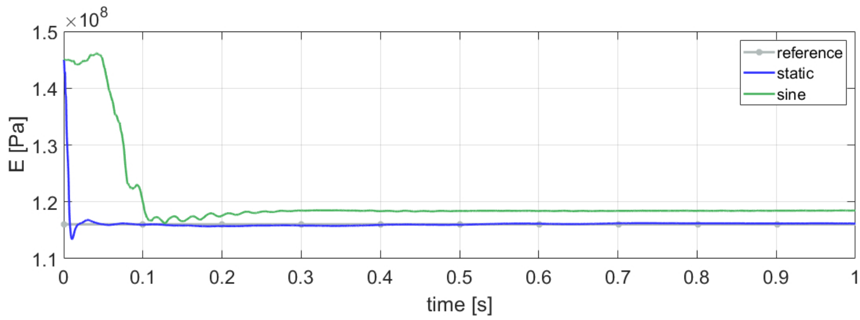

Figure 23: Estimated value of E with experimental data, for the static and sine load cases, with $\delta_E = 10^{-3}Hz$.

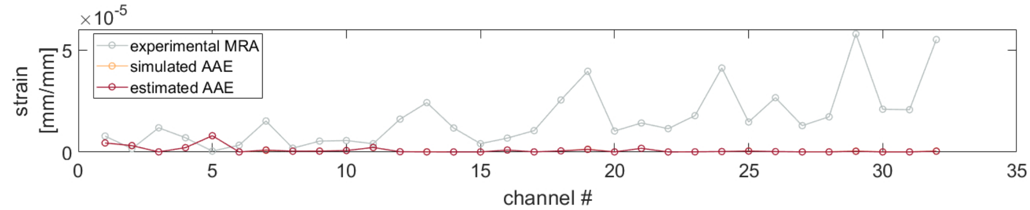

(a) Static load case

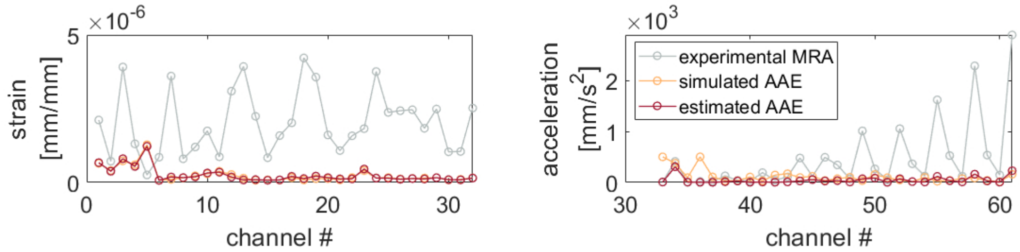

(b) Sine load case

Figure 24: Estimated sensor errors for the case shown in Figure 23.

6.1.2. Young's Modulus and Density

For the case where the Young's modulus and density are jointly estimated, with a known input, the augmented state covariance values are calculated by choosing $\delta_p = 1Hz$. The static load case leads to an unobservable system, hence only the sine load case is considered. The observed error has an average value of 1% for density and 3.45% for stiffness, which can be considered acceptable. The results are shown in Figure 25. As can be seen in Figure 26, the convergence of the ratio between the two parameters is quicker then for the single values. A small error for the full field of sensors can also be observed in this case, as shown in Figure 27. The larger required value for $\delta_p = 1Hz$ introduces more noise as well as a low frequency variation of the estimated parameter values. This could be attributed to a small model mismatch. This mismatch is assumed to be filtered out by the smaller value of $\delta_E = 10^{-3}Hz$ in the former case where only the Young's modulus is estimated.

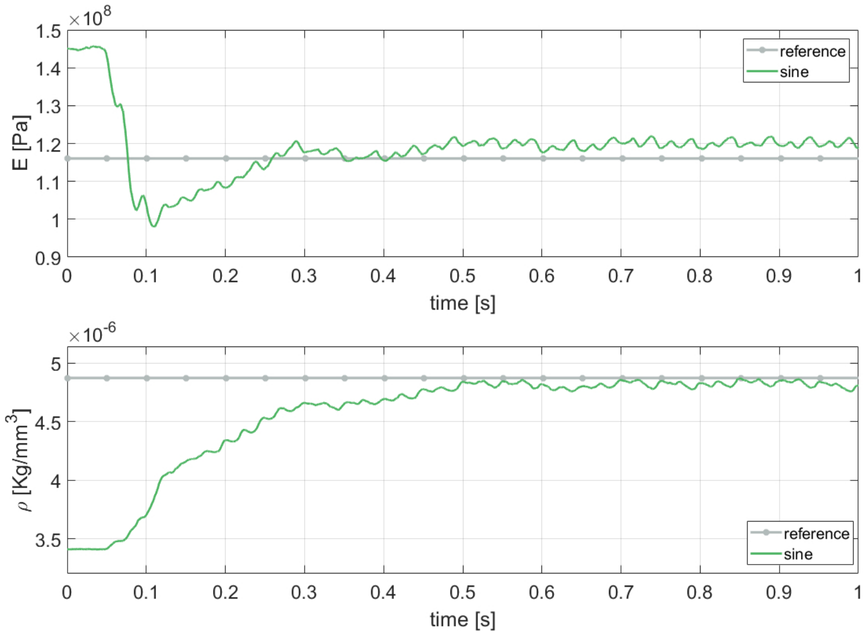

Figure 25: Estimated values of E and ρ with experimental data, for the sine load case, with $\delta_E = 1Hz$, $\delta_\rho = 1Hz$.

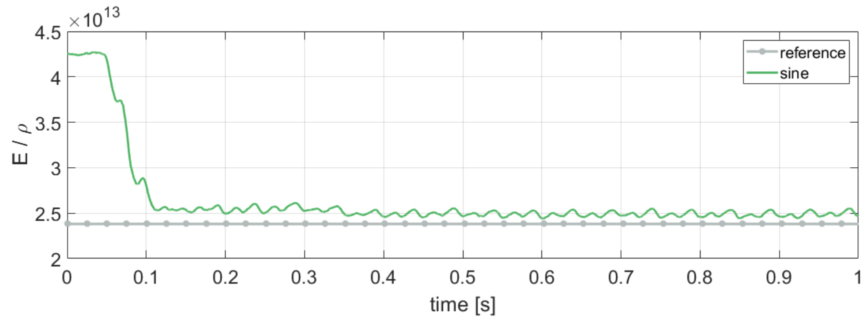

Figure 26: Value of the ratio between estimated E and ρ for the case shown in Figure 25.

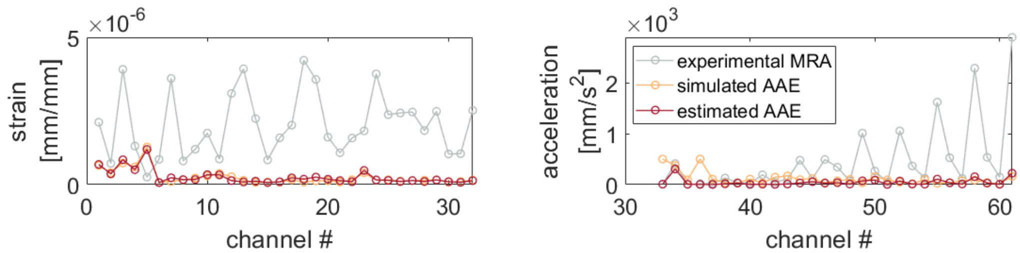

Figure 27: Estimated sensors error for the case shown in Figure 25.

6.2. Parameter and Input Estimation

For the joint estimation of the Young's modulus and an unknown input, the associated augmented state covariance values are calculated choosing $\delta_E = 10^{-3} Hz$ and $\omega_{u,2} = 80 Hz$. As the system is unobservable for a static load, the sine input load case is considered. An average error on the estimated Young's modulus below 1% can be observed, as shown in Figure 28. While the full field of strain sensors is accurately estimated, the acceleration estimated sensors exhibit a larger error as compared to the previous cases Figure 29. As explained above for the numerical case, this could be attributed to the high frequency load content introduced by the filter due to the larger augmented state covariance values.

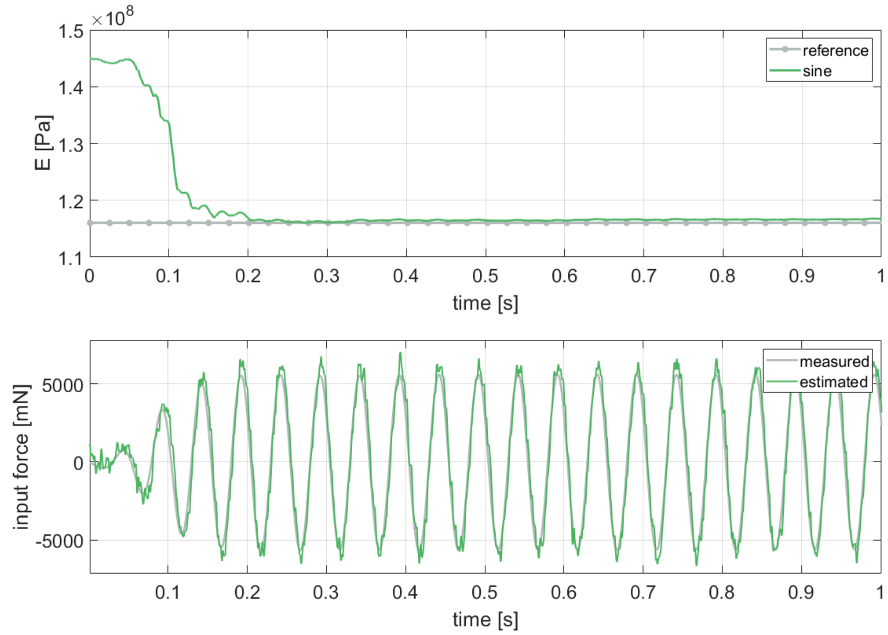

Figure 28: Estimated values of E and input with experimental data, for the sine load case, with $\delta_E = 10^{-3} Hz$ and $\omega_{u,2} = 80 Hz$.

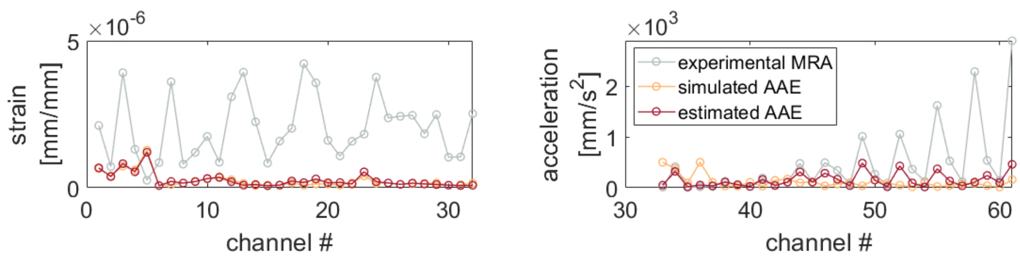

Figure 29: Estimated sensors error for the case shown in Figure 28.

7. Conclusions

In this work, the integration of a parametric Reduced Order Model (pROM) in an augmented Extended Kalman Filter (EKF) is presented, allowing for the joint estimation of states, inputs and material parameters of an industrial scale structural dynamic system. A projection-based parametric Model Order Reduction (pMOR) scheme that exploits the affine dependency on the parameters of the full model and uses a constant global reduction basis is proposed to achieve an efficient reduced model that maintains an explicit dependency on the parameters. The integration of the pROM in the EKF algorithm enables the efficient parameter estimation.

An observability analysis shows that in a general case a number of position-level measurements at least equal to the number of unknown inputs and parameters is required. Furthermore, several considerations on the observability of specific combinations of unknown mass and stiffness parameters and inputs are discussed.

The proposed methodology is applied to a scaled wind turbine blade. The pROM is numerically validated by comparing time and frequency results with a standard (i.e. non-parametric) Reduced Order Model (ROM). Estimation of parameters, inputs and states on both numerical and experimental data shows that the proposed approach is able to correctly estimate the unknown quantities together with the full field of strains and accelerations using a small set of strain sensors. Practical considerations on the setup of the filter are discussed, with a focus on the augmented state covariance values; these show how using an adapting scheme for the selection of covariance values would be helpful and should be explored in future research.

Future efforts will be aimed at estimating anisotropic constitutive material parameters, as well as developing an extended Optimal Sensor Placement (OSP) approach that considers the augmented states related to the material parameters.

Acknowledgments

This research was partially funded by POR Calabria 2014-2020 (Programma Operativo Regionale Calabria FESR-FSE 2014-2020, Asse 12 "Istruzione e formazione", Azione 10.5.6 e Azione 10.5.12).

This research was partially supported by Flanders Make, the strategic research centre for the manufacturing industry, within the ICON project VSFlex (Virtual Sensing on Flexible systems using distributed parameter models). VLAIO (Flanders Innovation & Entrepreneurship Agency) is also acknowledged for its support.

This research was partially supported by VLAIO (Flanders Innovation & Entrepreneurship Agency) within the O&O project IMPROVED (effIcient Model-based oPeRatiOnal VEhicle Dynamics testing)

The authors acknowledge 3D Systems Leuven for their cooperation in the creation of the hardware.

References

[1] J. Mottershead, M. Friswell, Model updating in structural dynamics: A survey, Journal of Sound and Vibration 167 (2) (1993) 347–375. doi:10.1006/jsvi.1993.1340.

[2] M. Friswell, J. Mottershead, Finite Element Model Updating in Structural Dynamics, Springer, Dordrecht, 1995. doi:10.1007/978-94-015-8508-8.

[3] A. K. S. Jardine, D. Lin, D. Banjevic, A review on machinery diagnostics and prognostics implementing condition-based maintenance, Mechanical Systems and Signal Processing 20 (2006) 1483–1510. doi:10.1016/j.ymssp.2005.09.012.

[4] C. R. Farrar, K. Worden, An introduction to structural health monitoring, Philosophical Transactions of the Royal Society 365 (2007) 303–315. doi:10.1098/rsta.2006.1928.

[5] R. E. Kalman, A new approach to linear filtering and prediction problems, Journal of Fluids Engineering, Transactions of the ASME 82 (1) (1960) 35–45. doi:10.1115/1.3662552.

[6] D. Simon, Optimal State Estimation: Kalman, Hinf and Nonlinear Approaches, Wiley, New York, 2006. doi:10.1002/0470045345.

[7] R. Van Der Merwe, Sigma-Point Kalman Filters for Probabilistic Inference in Dynamic State-Space Models, Oregon Health & Science University, 2004.

[8] H. Khodadadi, H. Jazayeri-Rad, Applying a dual extended Kalman filter for the nonlinear state and parameter estimations of a continuous stirred tank reactor, Computers and Chemical Engineering 35 (11) (2011) 2426–2436. doi:10.1016/j.compchemeng.2010.12.010.

[9] Y. Huang, J. Yu, J. Beck, H. Zhu, H. Li, Novel sparseness-inducing dual Kalman filter and its application to tracking time-varying spatially-sparse structural stiffness changes and inputs, Computer Methods in Applied Mechanics and Engineering 372 (2020). doi:10.1016/j.cma.2020.113411.

[10] E. Lourens, E. Reynders, G. De Roeck, G. Degrande, G. Lombaert, An augmented Kalman filter for force identification in structural dynamics, Mechanical Systems and Signal Processing 27 (1) (2012) 446–460. doi:10.1016/j.ymssp.2011.09.025.

[11] B. Forrier, Virtual torque sensing. A model-based approach for indirect measurement of dynamic operational loads on mechatronic powertrains, KU Leuven, 2018.

[12] F. Naets, J. Croes, W. Desmet, An online coupled state/input/parameter estimation approach for structural dynamics, Computer Methods in Applied Mechanics and Engineering 283 (2015) 1167–1188. doi:10.1016/j.cma.2014.08.010.

[13] R. Cumbo, T. Tamarozzi, K. Janssens, W. Desmet, Kalman-based load identification and full-field estimation analysis on industrial test case, Mechanical Systems and Signal Processing 117 (2019) 771–785. doi:10.1016/j.ymssp.2018.08.045.

[14] F. Naets, J. Cuadrado, W. Desmet, Stable force identification in structural dynamics using Kalman filtering and dummy-measurements, Mechanical Systems and Signal Processing 50-51 (2015) 235–248. doi:10.1016/j.ymssp.2014.05.042.

[15] E. Risaliti, T. Tamarozzi, M. Vermaut, B. Cornelis, W. Desmet, Multibody model based estimation of multiple loads and strain field on a vehicle suspension system, Mechanical Systems and Signal Processing 123 (2019) 1–25. doi:10.1016/j.ymssp.2018.12.024.

[16] A. Corigliano, S. Mariani, Parameter identification in explicit structural dynamics: Performance of the extended Kalman filter, Computer Methods in Applied Mechanics and Engineering 193 (36-38) (2004) 3807–3835. doi:10.1016/j.cma.2004.02.003.

[17] R. Astroza, A. Alessandri, Effects of model uncertainty in nonlinear structural finite element model updating by numerical simulation of building structures, Structural Control and Health Monitoring 26 (3) (2019) 1–32. doi:10.1002/stc.2297.

[18] M. Song, R. Astroza, H. Ebrahimian, B. Moaveni, C. Papadimitriou, Adaptive Kalman filters for nonlinear finite element model updating, Mechanical Systems and Signal Processing 143 (2020) 106837. doi:10.1016/j.ymssp.2020.106837.

[19] V. K. Dertimanis, E. N. Chatzi, S. Eftekhar Azam, C. Papadimitriou, Input-state-parameter estimation of structural systems from limited output information, Mechanical Systems and Signal Processing 126 (2019) 711–746. doi:10.1016/j.ymssp.2019.02.040.

[20] Y. Lei, X. Li, J. Huang, L. Liu, Simultaneous Assessment of Damage and Unknown Input for Large Structural Systems by UKF-UI, Journal of Engineering Mechanics 147 (2021). doi:10.1061/(ASCE)EM.1943-7889.0001981.

[21] M. Impraimakis, A. W. Smyth, An unscented Kalman filter method for real time input-parameter-state estimation, Mechanical Systems and Signal Processing 162 (March 2021) (2022) 108026. doi:10.1016/j.ymssp.2021.108026.

[22] W. H. A. Schilders, H. van der Vorst, J. Rommes, Model Order Reduction: Theory, Research Aspects and Applications, Springer, Berlin, Heidelberg, 2008. doi:10.1007/978-3-540-78841-6.

[23] B. Besselink, U. Tabak, A. Lutowska, N. Van De Wouw, H. Nijmeijer, D. J. Rixen, M. E. Hochstenbach, W. H. Schilders, A comparison of model reduction techniques from structural dynamics, numerical mathematics and systems and control, Journal of Sound and Vibration 332 (19) (2013) 4403–4422. doi:10.1016/j.jsv.2013.03.025.

[24] A. Quarteroni, A. Manzoni, F. Negri, Reduced basis methods for partial differential equations: An

introduction, Springer, Cham, 2015. doi:10.1007/978-3-319-15431-2.
[25] P. Benner, S. Gugercin, K. Willcox, A survey of projection-based model reduction methods for parametric dynamical systems, SIAM Review 57 (4) (2015) 483–531. doi:10.1137/130932715.
[26] X. Xie, H. Zheng, S. Jonckheere, B. Pluymers, W. Desmet, A parametric model order reduction technique for inverse viscoelastic material identification, Computers and Structures 212 (2019) 188–198. doi:10.1016/j.compstruc.2018.10.013.
[27] K. Agathos, K. E. Tatsis, K. Vlachas, E. Chatzi, Parametric reduced order models for output-only vibration-based crack detection in shell structures, Mechanical Systems and Signal Processing 162 (2021) 108051. doi:10.1016/j.ymssp.2021.108051.
[28] W. Bova, E. Lappano, P. G. Catera, D. Mundo, Development of a parametric model order reduction method for laminated composite structures, Composite Structures 243 (2020) 112219. doi:10.1016/j.compstruct.2020.112219.
[29] T. Tamarozzi, G. H. Heirman, W. Desmet, An on-line time dependent parametric model order reduction scheme with focus on dynamic stress recovery, Computer Methods in Applied Mechanics and Engineering 268 (2014) 336–358. doi:10.1016/j.cma.2013.09.021.
[30] D. Cook, D. Malkus, M. Plesha, R. Witt, Concepts and Applications of Finite Element Analysis, Wiley, New York, 2001.
[31] E. Lappano, F. Naets, W. Desmet, D. Mundo, E. Nijman, A greedy sampling approach for the projection basis construction in parametric model order reduction for structural dynamics models, Proceedings of ISMA 2016 - International Conference on Noise and Vibration Engineering (2016) 3563–3571.
[32] Siemens simcenter 3d.
URL https://www.plm.automation.siemens.com/global/en/products/simcenter/
[33] D. Amsallem, C. Farhat, Stabilization of projection-based reduced-order models, International Journal for Numerical Methods in Engineering 91 (2012) 358–377. doi:10.1002/nme.4274.
[34] A. van de Walle, F. Naets, E. Deckers, W. Desmet, Stability-preserving model order reduction for time-domain simulation of vibro-acoustic FE models, International Journal for Numerical Methods in Engineering 109 (2017) 889–912. doi:10.1002/nme.5323.
[35] Y. Yang, T. Nagayama, K. Xue, Structure system estimation under seismic excitation with an adaptive extended kalman filter, Journal of Sound and Vibration 489 (2020) 115690. doi:10.1016/j.jsv.2020.115690.
[36] M. Cheng, T. C. Becker, Performance of unscented Kalman filter for model updating with experimental data, Earthquake Engineering and Structural Dynamics 50 (7) (2021) 1948–1966. doi:10.1002/eqe.3426.
[37] R. Cumbo, L. Mazzanti, T. Tamarozzi, P. Jiranek, W. Desmet, F. Naets, Advanced optimal sensor placement for Kalman-based multiple-input estimation, Mechanical Systems and Signal Processing 160 (2021) 107830. doi:10.1016/j.ymssp.2021.107830.
[38] M. Hautus, Controllability and observability condition of linear autonomous systems, Nederlandse Akademie van Wetenschappen. Proceedings. Series A. Indagationes Mathematicae (1969).
[39] B. K. Ghosh, J. Rosenthal, A Generalized Popov-Belevitch-Hautus Test of Observability, IEEE Transactions on Automatic Control 40 (1) (1995) 176–180. doi:10.1109/9.362874.
[40] F. Naets, R. Pastorino, J. Cuadrado, W. Desmet, Online state and input force estimation for multibody models employing extended Kalman filtering, Multibody System Dynamics 32 (3) (2014) 317–336. doi:10.1007/s11044-013-9381-8.
[41] E. Risaliti, B. Cornelis, T. Tamarozzi, W. Desmet, A state-input estimation approach for force identification on an automotive suspension component, Conference Proceedings of the Society for Experimental Mechanics Series 3 (2016) 359–369. doi:10.1007/978-3-319-29754-5_35.
[42] G. Brzhezinski, S. Vettori, E. Di Lorenzo, B. Peeters, E. Chatzi, F. Cosco, On the dynamic virtualization of a 3d-printed scaled wind turbine blade, in: Proceedings of 40th IMAC Conference, 2022.